

# Supplementary Information for: Weak, Seismogenic Faults Inherited From Mesozoic Rifts Control Mountain Building in the Andean Foreland

Sam Wimpenny<sup>1\*</sup>

<sup>1</sup>COMET, Bullard Laboratories, Department of Earth Sciences,  
University of Cambridge, UK

\*email: *sew57@cam.ac.uk*

1 This Supplementary Information contains:

- 2     • **Text S1:** A description of the body-waveform modelling methods.
- 3     • **Supplementary Table 1:** A table of earthquake locations, magnitudes, centroid depths and  
4       mechanisms derived in this study.
- 5     • **Text S2:** Numerical scheme used to solve for the temperature structure in rifted lithosphere.
- 6     • **Text S3:** Relationship between earthquakes, subducting slab depth and foreland lithosphere  
7       thickness along the margin of the Andes.
- 8     • **Supplementary Figures 4-50:** Fits between synthetic and observed waveforms for each earth-  
9       quake studied using body-waveform modelling.

## Text S1: Earthquake Seismology Methods

### Long-Period Waveform Modelling

I first selected broadband seismograms at stations between 30 and 90 epicentral degrees from the source from the IRIS data management centre, rotated the seismograms and picked the  $P$  and  $SH$  arrival times by hand. I then filtered the seismograms to the response of a long-period World Wide Standardised Seismograph Network instrument (15-100 s). Within this period band,  $M_w \lesssim 7.5$  earthquakes can be treated as a point in space, and the waveform shapes are simply related to the fault geometry, centroid depth and source-time function [Nabalek, 1984; McCaffrey and Abers, 1988].

Up to 50 seismograms that provide good azimuthal coverage of the focal sphere were then selected for waveform modelling. By only matching the shape of the seismograms, and not the absolute phase travel times, the modelling procedure is insensitive to the velocity structure along the direct path between the earthquake and receiver. The shapes of the long-period waveforms are also relatively insensitive to the small-scale heterogeneity in the velocity structure above the earthquake centroid [Taymaz et al., 1990]. Earthquake centroid depths, however, are sensitive to the average velocity of the material above the earthquake source, as they are constrained by the differential travel time between the direct and depth phases. I use a simple 1-D velocity model consistent with previous studies that has  $V_p = 6.5$  km/s and  $V_s = 3.7$  km/s in the crust and  $V_p = 8.1$  km/s and  $V_s = 4.5$  km/s in the mantle [e.g. Devlin et al., 2012; James and Snoke, 1994; Suárez et al., 1990; Ojeda and Havskov, 2001], with crustal thickness constrained by nearby receiver function estimates. I discuss the uncertainties in centroid depths associated with velocity model errors below.

I performed iterative, weighted least-squares inversions of the long-period waveforms for the earthquake source parameters using the MT5 program of Zwick et al. [1994]. All earthquakes are constrained to have a pure double-couple source mechanism, and the starting mechanism used in the inversion is typically the best double-couple mechanism derived by the global Centroid Moment Tensor catalogue (gCMT) [Dziewonski et al., 1981; Ekström et al., 2012]. Seismograms are weighted in the inversion by their azimuthal density to limit over-fitting of a few clustered stations, which is often the case due to limited station coverage in the Atlantic and Pacific Oceans. The  $P$ -waves are also weighted by twice as much as the  $SH$ -waves to account for differences in their amplitudes on long-period seismograms.

When a minimum-misfit solution was found, I performed sensitivity tests by fixing each parameter of interest away from its optimum value and performing inversions to see how the waveform fits change as a function of each parameter. I found that the strike, dip and rake are typically constrained to within  $\pm 20^\circ$ ,  $\pm 10^\circ$  and  $\pm 20^\circ$ , respectively. These uncertainties are slightly larger than typical for this method [c.f. Abers and McCaffrey, 1988; Taymaz et al., 1990], owing to the poor azimuthal distribution of teleseismic stations in South America. Earthquake centroid depths are typically constrained to within  $\pm 2$ – $4$  km by the waveform shapes depending on the event depth and magnitude. Earthquakes shallower than 10–15 km can have larger uncertainties due to the trade-off between source-time function length and centroid depth [Christensen and Ruff, 1985].

## 47 Broadband and Short-Period Waveform Modelling

48 Earthquakes that are  $4.9 < M_w < 5.4$  do not generate significant energy in the 15-100 s period  
 49 band at enough teleseismic stations to use the long-period method described above. However, the  
 50  $P$ ,  $pP$  and  $sP$  phases are often clear on a small number of vertical-component broadband or short-  
 51 period seismograms, and their relative timing and amplitudes can be used to determine the earthquake  
 52 centroid depth and place loose constraints on the focal mechanism [e.g. Forsyth, 1982]. For earthquakes  
 53 of this magnitude, the direct and depth phases recorded on broadband seismometers can be modelled  
 54 as an impulse rupture at a point source in space [Maggi et al., 2000].

55 I first selected vertical-component seismograms from the IRIS data management centre and picked  
 56 the arrival time and polarity of the direct  $P$ -wave. For a small number of stations ( $<8$ ) where the  
 57 direct arrival and depth phases are clear, I then calculated synthetic seismograms using the gCMT  
 58 focal mechanism for a range of candidate depths by ray tracing through the ak135 velocity model  
 59 of Kennett et al. [1995] using the WKB method of Chapman [1978]. The depth of the Moho in  
 60 the ak135 model was adjusted to crustal thickness estimates from receiver functions where available.  
 61 Attenuation was modelled using the  $t^*$  operator of Futterman [1962], with the value of  $t^*$  being varied  
 62 to match the width of the observed waveforms. The observed and synthetic waveforms were aligned  
 63 on the first peak after the  $P$ -wave arrival and the best-fit depth was found by matching the relative  
 64 arrival times of the direct and depth phases. The fit between the observed and synthetic seismograms  
 65 typically constrained the centroid depth to within  $\pm 1$ –2 km.

66 If the earthquake depth phases are of similar amplitude to the noise levels in the  $P$ -wave coda, then  
 67 the signal-to-noise ratio can be enhanced by stacking multiple seismograms. Small-aperture arrays  
 68 contain multiple seismometers with small enough spacing that their seismograms can be coherently  
 69 stacked using a simple time-shift based on the horizontal slowness and back-azimuth of the direct  
 70  $P$ -wave. I used the method of Heyburn and Bowers [2008] to stack short-period seismograms from  
 71 small-aperture array sites in North America and Europe to extract coherent depth-phase energy from  
 72 the  $P$ -wave coda [see also Craig et al., 2012]. The depth of the event was determined by fitting  
 73 synthetic seismograms to the stacked and bandpass-filtered seismogram. The waveform matching  
 74 could typically be performed to within  $\sim 0.5$  s, and the centroid depth determined to within  $\pm 1$ –2 km.

## 75 Centroid Depth Uncertainties Due to Velocity Structure

76 Errors in the velocity structure overlying the source will contribute additional uncertainty to the  
 77 centroid depth estimates. Local earthquake surveys along the margins of the Andes indicate the  
 78 crystalline crust at depths of 10–30 km has  $V_p$  between 6.0 km/s and 6.7 km/s, increasing to  $\sim 7$  km/s  
 79 at depths of 30–40 km [Smalley and Isacks, 1990; Dorbath et al., 1991; James and Snoke, 1994; Ojeda  
 80 and Havskov, 2001]. Therefore, an average  $V_p$  of 6.5 km/s may include  $\pm 5$ –10% uncertainty, which  
 81 translates roughly linearly into  $\pm 5$ –10% uncertainty in the centroid depth estimates ( $\pm 1$ –2 km for 20  
 82 km centroid depth). Beneath the foreland basin the depth to crystalline crust can locally reach up to  
 83 10 km, though the average is 2–5 km [McGroder et al., 2015]. Foreland sediments have average  $V_p$  of  
 84 4–5 km/s and  $V_s$  of 2–3 km/s. Therefore, given that the sediment layer is typically  $< 5$  km thick, then  
 85 the centroid depth errors introduced by ignoring the sediments will be  $< 2$  km.

For earthquakes in the upper mantle, uncertainty in the position of the Moho relative to the earthquake centroid will lead to uncertainty in the centroid depth. The depth of Moho has been studied extensively using the receiver function method in the Andean forelands, which have uncertainties of  $\pm 2\text{--}4$  km [e.g. Poveda et al., 2015; Ryan et al., 2016; Condori et al., 2017]. For an upper-mantle earthquake, uncertainty in the Moho depth will translate into  $\pm 1\text{--}2$  km uncertainty in the centroid depth.

## Local and Regional Earthquake Surveys

Microseismicity recorded by temporary seismometer networks provide a complimentary source of earthquake depths. In particular, the small earthquakes captured by the local networks are far more frequent than moderate-magnitude earthquakes, and can illuminate the depth distribution of seismicity in more detail. I used seismicity located by networks from San Juan in Argentina [Smalley and Isacks, 1990; Smalley et al., 1993], Jujuy in Argentina [Cahill et al., 1992], Shira in Peru [Dorbath et al., 1986; Suárez et al., 1990; Dorbath et al., 1991], Cutucu in Ecuador [Legrand et al., 2005] and Tauramana in Colombia [Dimate et al., 2003]. The depth sensitivity of these local surveys depends on the event location, the station distribution and the accuracy of the velocity model. Conservative bounds would suggest the event depths may be uncertain by up to 10 km [e.g. Suárez et al., 1990].

I also used the depths of earthquakes in Ecuador and Argentina derived using regional waveform modelling by Vaca et al. [2019] and Alvarado et al. [2005], respectively. Both studies used waveforms with periods between 15 s and 100 s and quote depth uncertainties of  $\sim 2\text{--}3$  km, though events outside of the network can have broad misfit minima leading to uncertainties of  $\sim 10$  km.

Date	Time	Lon	Lat	waveform modelling				global CMT				$M_w$	Ref
				$z$	$s$	$d$	$r$	$s$	$d$	$r$	$\gamma$		
19870306	0410	-77.84	0.07	$22^{+5}_{-5}$	-	-	-	195	27	98	99	7.1	b
19921226	1457	-78.06	-1.03	$8^{+3}_{-2}$	-	-	-	200	46	166	45	5.8	b
19940531	2046	-72.12	7.83	$13^{+2}_{-1}$	-	-	-	137	45	54	98	5.4	d
19941109	0357	-71.73	7.53	$8^{+1}_{-1}$	-	-	-	178	42	113	78	5.4	d
19950423	2355	-72.49	5.20	$8^{+3}_{-2}$	-	-	-	67	52	133	75	5.2	d
19951007	2128	-77.80	-2.83	$12^{+2}_{-3}$	$133^{+15}_{-20}$	$39^{+10}_{-5}$	$34^{+15}_{-15}$	161	22	33	86	5.8	B
20000117	1220	-72.00	6.72	$14^{+1}_{-1}$	-	-	-	154	26	71	98	5.6	d
20001008	2012	-78.10	0.36	$13^{+1}_{-1}$	-	-	-	342	42	90	94	5.1	d
20011221	2051	-70.92	8.13	$13^{+2}_{-4}$	$226^{+15}_{-25}$	$64^{+15}_{-25}$	$158^{+15}_{-20}$	230	60	164	58	5.5	B
20020504	1251	-64.55	-23.12	$13^{+1}_{-1}$	-	-	-	180	21	79	72	5.2	d
20040328	0123	-73.57	-10.18	$32^{+2}_{-2}$	171	18	90	171	22	93	83	5.2	D
20060221	2100	-75.51	-10.28	$8^{+1}_{-1}$	131	20	44	131	24	44	94	5.1	D
20060805	1403	-68.76	-33.12	$23^{+2}_{-2}$	-	-	-	137	39	44	70	5.6	d
20080626	0006	-75.64	-8.91	$5^{+1}_{-1}$	-	-	-	249	41	106	96	5.2	d
20080701	0017	-75.56	-10.39	$6^{+1}_{-1}$	-	-	-	148	38	66	95	5.4	d
20090311	1306	-69.19	-31.92	$26^{+2}_{-2}$	-	-	-	190	44	109	80	5.3	d
20091009	1811	-77.87	-1.05	$9^{+1}_{-1}$	-	-	-	204	46	105	83	5.2	d
20100119	1728	-65.76	-27.56	$33^{+2}_{-2}$	-	-	-	243	75	178	87	5.2	d
20100123	0940	-63.92	-17.58	$12^{+2}_{-2}$	-	-	-	-	-	-	-	4.9	d*
20110221	0658	-64.68	-27.14	$16^{+1}_{-1}$	-	-	-	184	34	108	89	5.6	d
20111013	1506	-75.66	-6.63	$7^{+1}_{-1}$	-	-	-	162	41	104	96	5.2	d
20121025	2049	-76.17	-5.94	$23^{+2}_{-2}$	106	32	102	106	32	112	95	5.2	D
20131115	0619	-67.51	-32.66	$25^{+2}_{-2}$	-	-	-	208	41	103	94	5.2	d
20140219	1110	-69.67	9.61	$9^{+1}_{-1}$	-	-	-	240	63	153	84	5.3	d
20150709	1808	-75.70	-9.16	$24^{+2}_{-2}$	-	-	-	2	34	111	96	5.2	d
20150801	1130	-68.36	-30.05	$15^{+1}_{-1}$	-	-	-	166	29	102	89	5.2	d
20151017	1133	-64.53	-25.42	$20^{+2}_{-2}$	$321^{+30}_{-30}$	$35^{+20}_{-10}$	$48^{+40}_{-20}$	312	43	41	69	5.8	B
20151113	0604	-64.50	-29.81	$26^{+2}_{-2}$	$313^{+30}_{-30}$	$24^{+10}_{-5}$	$71^{+30}_{-20}$	343	21	99	92	5.6	B
20160522	1220	-64.31	-22.36	$8^{+1}_{-1}$	195	60	160	210	37	137	96	5.3	D
20161031	0020	-74.63	3.37	$40^{+2}_{-4}$	-	-	-	213	51	131	85	5.6	b
20161212	0256	-67.95	-30.89	$15^{+1}_{-1}$	8	50	90	8	51	132	99	5.1	D
20170206	1302	-74.67	3.45	$44^{+3}_{-3}$	-	-	-	217	43	118	86	5.4	d
20170220	0745	-74.97	-5.21	$26^{+2}_{-2}$	-	-	-	186	40	94	99	5.1	d
20170813	1651	-74.60	-10.70	$33^{+1}_{-2}$	$310^{+30}_{-10}$	$42^{+20}_{-20}$	$16^{+30}_{-30}$	313	52	1	80	5.7	B

**Supplementary Table 1:** Earthquake source parameters derived from waveform modelling in this study. Locations are taken from the ISC-EHB catalogue where available [Weston et al., 2018], otherwise the centroid location is taken from the gCMT catalogue [Ekström et al., 2012].  $z$ ,  $s$ ,  $d$  and  $r$  are the centroid depth, strike, dip and rake, and  $\gamma$  is the % double-couple of the gCMT moment tensor as defined by Jackson et al. [2002]. Events marked with a *B* in the Ref column were studied using long-period waveform modelling. Events marked *D* were studied using broadband or short-period waveform modelling. A lower case letter indicates only the depth was solved for. Events marked with a \* did not have a gCMT focal mechanism. The table is continued on the next page.

Date	Time	Lon	Lat	waveform modelling				global CMT				$M_w$	Ref
				$z$	$s$	$d$	$r$	$s$	$d$	$r$	$\gamma$		
20180719	0539	-74.61	3.42	$49^{+2}_{-2}$	-	-	-	12	57	149	94	4.9	d
20190214	1433	-74.33	-12.18	$22^{+2}_{-2}$	49	79	94	153	42	103	95	5.6	D
20190217	1322	-64.45	-23.66	$10^{+1}_{-1}$	-	-	-	187	34	85	93	5.1	d
20191119	2310	-66.88	-33.64	$14^{+2}_{-3}$	$207^{+20}_{-40}$	$46^{+5}_{-5}$	$60^{+15}_{-10}$	213	47	61	59	5.7	B
20191224	1903	-74.05	3.50	$12^{+2}_{-2}$	$193^{+20}_{-20}$	$53^{+10}_{-5}$	$126^{+15}_{-10}$	208	67	154	99	5.9	B
20200507	0049	-76.70	-5.73	$34^{+2}_{-2}$	-	-	-	288	37	48	88	5.3	d
20200712	1508	-69.86	9.41	$17^{+2}_{-2}$	-	-	-	154	71	39	99	5.1	d
20201030	1824	-75.18	-10.18	$37^{+3}_{-2}$	160	55	100	169	43	102	60	5.5	b
20210119	0246	-68.85	-31.81	$22^{+3}_{-4}$	$228^{+20}_{-15}$	$67^{+10}_{-5}$	$151^{+15}_{-25}$	223	61	164	94	6.4	B
20210209	0141	-77.19	-5.40	$22^{+2}_{-2}$	-	-	-	-	-	-	-	5.0	d*
20210322	0437	-71.36	3.90	$6^{+1}_{-1}$	-	-	-	86	52	-73	-	5.1	d
20211010	0020	-71.71	-11.74	$7^{+5}_{-3}$	92	50	-61	116	51	-49	-	5.6	b*

105 (cont.) Supplementary Table 1

## Text S2: Numerical Scheme used to Model Mesozoic Rifting

I modelled the thermal evolution of the lithosphere assuming that rifting can be approximated by pure-shear thinning following McKenzie [1978]. The temperature within the lithosphere and underlying asthenospheric mantle is governed by the 1-D advection-diffusion equation with internal radiogenic heating subject to a surface and basal temperature boundary condition. The equation is formulated in a Lagrangian reference frame to simplify the treatment of vertical advection:

$$\frac{D(\rho C_p T)}{Dt} = \frac{\partial}{\partial x} \left( k \frac{\partial T}{\partial x} \right) + H, \quad (1)$$

where  $D/Dt$  is the Lagrangian differential operator,  $k(T, X)$  is the thermal conductivity,  $H(X)$  is the radiogenic heat production,  $\rho(T, X)$  is the density and  $C_p(T, X)$  is the specific heat capacity, with these parameters being dependent on temperature  $T$  and composition  $X$ . Given the temperature-dependence of the material properties, this equation requires numerical solution. I integrated Equation 1 using an implicit Crank-Nicolson numerical scheme that is formulated using conservative finite differences on a staggered grid [Bown and White, 1995]. The full finite difference equations in which the superscripts are the time index  $n$  and the subscripts are the spatial index  $j$  are as follows:

$$R(T_j^{n+1} - T_j^n) = \frac{1}{\Delta x_{j+1}^{n+1} + \Delta x_j^{n+1}} \left[ \frac{k_{j+1/2}^{n+1}}{\Delta x_{j+1}^{n+1}} (T_{j+1}^{n+1} - T_j^{n+1}) - \frac{k_{j-1/2}^{n+1}}{\Delta x_j^{n+1}} (T_j^{n+1} - T_{j-1}^{n+1}) \right] + \frac{1}{\Delta x_{j+1}^n + \Delta x_j^n} \left[ \frac{k_{j+1/2}^n}{\Delta x_{j+1}^n} (T_{j+1}^n - T_j^n) - \frac{k_{j-1/2}^n}{\Delta x_j^n} (T_j^n - T_{j-1}^n) \right] + H_j \quad (2)$$

where

$$\begin{aligned} R &= \frac{1}{2\delta t} (\rho_j^{n+1} C_p^{n+1} + \rho_j^n C_p^n) \\ \Delta x_{j+1}^i &= x_{j+1}^i - x_j^i \\ \Delta x_j^i &= x_j^i - x_{j-1}^i \end{aligned} \quad (3)$$

where  $\delta t$  is the time increment.

Equation 2 can be written in the form  $A.x^{n+1} = B.x^n + d$  and solved using tri-diagonal elimination. The solution is slightly non-linear but can be determined through iteration using a predictor-corrector step [e.g. McKenzie et al., 2005]. I used an initial spatial step  $\delta x$  of 1 km and a temporal step  $\delta t$  of 100,000 years. This discretisation satisfies the Courant stability condition  $\delta t < \min(5\rho C_p \delta x^2 / k)$  to ensure that heat diffusion between the nodes in one time step is much smaller than the node spacing. The model was benchmarked against an analytical steady-state solution for a three layer lithosphere with constant material parameters, and resolution tested at smaller  $\delta x$  and  $\delta t$  to ensure stability of the numerical scheme within the parameter range of interest.

## Material Parameters

The material parameters and boundary conditions used are shown in Supplementary Figure 1. The crust is separated into an upper and lower crust with constant values for density, specific heat capac-

ity, thermal conductivity and radiogenic heat production. The radiogenic heat producing elements are assumed to be mostly concentrated within the upper crust [e.g. Mareschal and Jaupart, 2013]. For the lithospheric mantle the material properties are assumed to be dependent on temperature using the calibrations proposed by McKenzie et al. [2005] and Grose and Afonso [2013]. The density parametrisation is as follows:

$$\rho(T) = \rho_0 \exp(\alpha_0 T + 0.5\alpha_1 T^2), \quad (4)$$

where  $\rho_0 = 3300 \text{ kg/m}^3$ ,  $\alpha_0 = 2.832 \times 10^{-5}$  and  $\alpha_1 = 0.758 \times 10^{-8}$  based on the model of Bouhifd et al. [1996] for olivine. The specific heat capacity parametrisation is as follows:

$$Cp = c_1 - c_2 T^{-0.5} - c_3 T^{-3}, \quad (5)$$

where  $c_1 = 1580$ ,  $c_2 = 12230$  and  $c_3 = 1694 \times 10^3$  taken from the parametrisation of Grose and Afonso [2013]. The thermal conductivity parametrisation is as follows:

$$\begin{aligned} k &= k_{rad} + k_{lat} \\ k_{lat} &= \frac{b_1}{1 + b_2 T} + b_3 + b_4 T + b_5 T^2 + b_6 T^3 \\ k_{rad} &= d_1 - d_2 + d_3 T - d_4 T^3 \end{aligned} \quad (6)$$

where  $d_1 = 0.0175$ ,  $d_2 = 0.000103$ ,  $d_3 = 2.245 \times 10^{-7}$ ,  $d_4 = 3.407 \times 10^{-11}$  and  $b_1 = 5.3$ ,  $b_2 = 0.0015$ ,  $b_3 = 1.753 \times 10^{-2}$ ,  $b_4 = -1.0365 \times 10^{-4}$ ,  $b_5 = 2.2451 \times 10^{-7}$ ,  $b_6 = -3.4071 \times 10^{-11}$  from the parametrisation of McKenzie et al. [2005].

## Sediment-Loaded Subsidence History

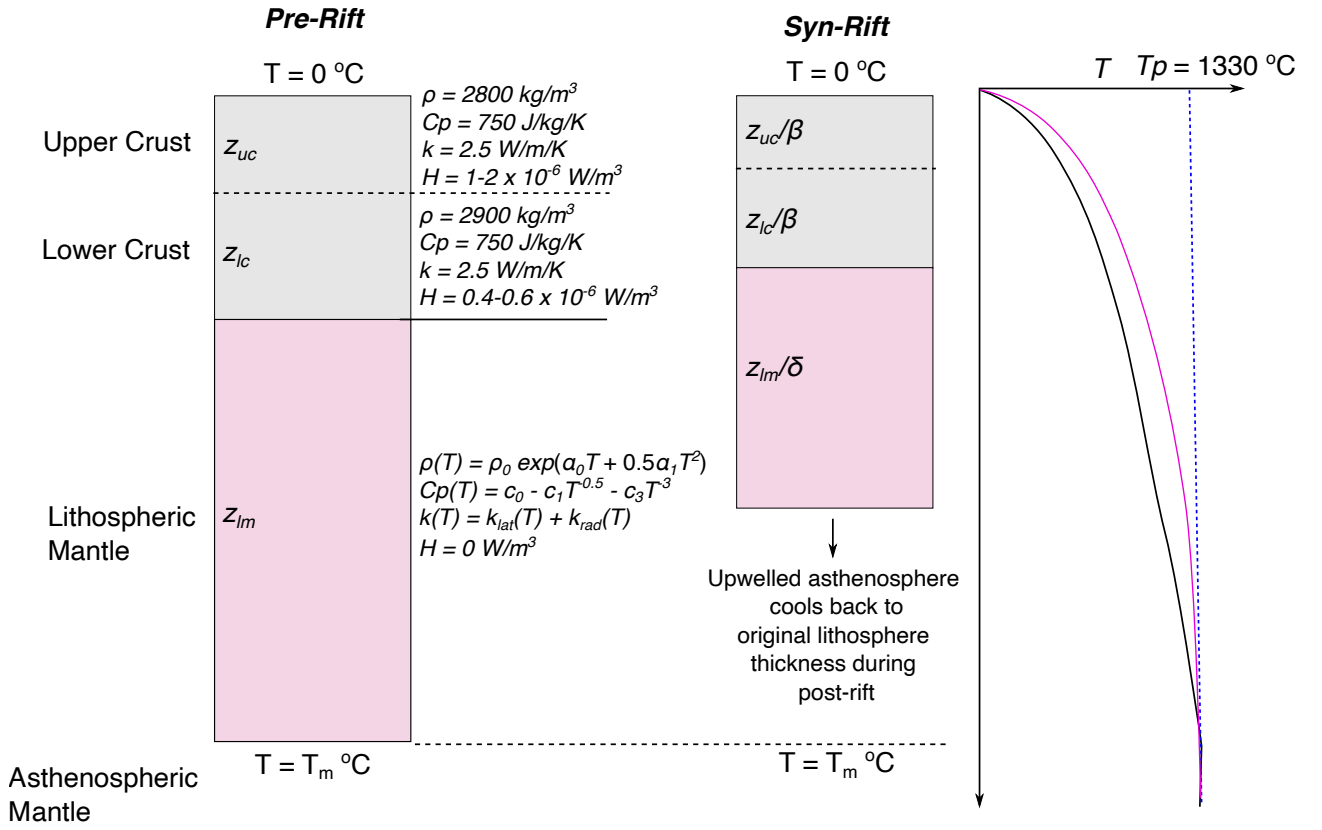
The sediment-loaded subsidence  $S_m$  for a particular model run is calculated by performing an isostatic balance between the rifting and pre-rift column of lithosphere, assuming that the basin is filled to capacity with sediment of density  $\rho_s = 2400 \text{ kg/m}^3$ :

$$S_m = \frac{1}{\rho_s - \rho_0} [P_{pr} - P_{sr} - \rho_0(z_{pr} - z_{sr})], \quad (7)$$

where  $P_{pr}$  and  $P_{sr}$  are the pressure at the base of the pre-rifted lithosphere of thickness  $z_{pr}$  and the syn-rift lithosphere of thickness  $z_{sr}$ . The pressure is calculated using numerical integration. All of the material parameters are shown in Supplementary Figure 1.

Although the sediment-loaded subsidence is calculated, the thermal effects of sediment blanketing were not included in the modelling. Simple steady-state calculations including a sediment layer indicated that the effects of sediment blanketing were small compared to the unknowns associated with crustal heat production, and led to small  $<50^\circ\text{C}$  temperature changes within the lower crust [Sandiford, 1999].





**Supplementary Figure 1:** Sketch of the rift model set-up. The column on the left shows the pre-rift configuration of the lithosphere with the material parameters that control the thermal and subsidence evolution of the lithosphere. The column on the right shows the configuration immediately following the end of rifting. The crust thins by a factor  $\beta$ , whilst the lithospheric mantle is allowed to thin by a factor  $\delta$ , which allows for an increase in temperature throughout the crust during rifting.

## Constraints on the Salta Rift Model

The four constraints on the model of the Salta Rift are come from the xenolith thermobarometry, sediment subsidence history and crust and mantle lithosphere thickness. I also constrain the onset of rifting to be no older than 100 Myrs based on the age of pre-rift sediments within the Salta Rift [Salfity and Marquillas, 1994]. The xenolith thermobarometry constraint is defined as:

$$800^\circ\text{C} < T < 900^\circ\text{C} \quad \text{at} \quad z \leq z_c \quad \text{and} \quad 80\text{Myrs} \leq t \leq 90\text{Myrs}, \quad (8)$$

where  $z_c$  is the crustal thickness at time  $t$ . The sediment-loaded subsidence history constraint is defined as:

$$\chi^2 = \sum \left[ \frac{S_m - S_s}{\sigma_s} \right]^2 \leq 3, \quad (9)$$

where  $S_m$  is the modelled sediment-loaded subsidence history,  $S_s$  is the observed sediment-loaded subsidence history and  $\sigma_s$  is an estimate of the uncertainties in the sediment thickness through time.  $\sigma_s$  is assumed to be 200 m based on the results of using different porosities and compaction length-scales when decompacting the subsidence history of Starck [2010]. Finally, the crust and lithospheric

mantle thickness is defined as:

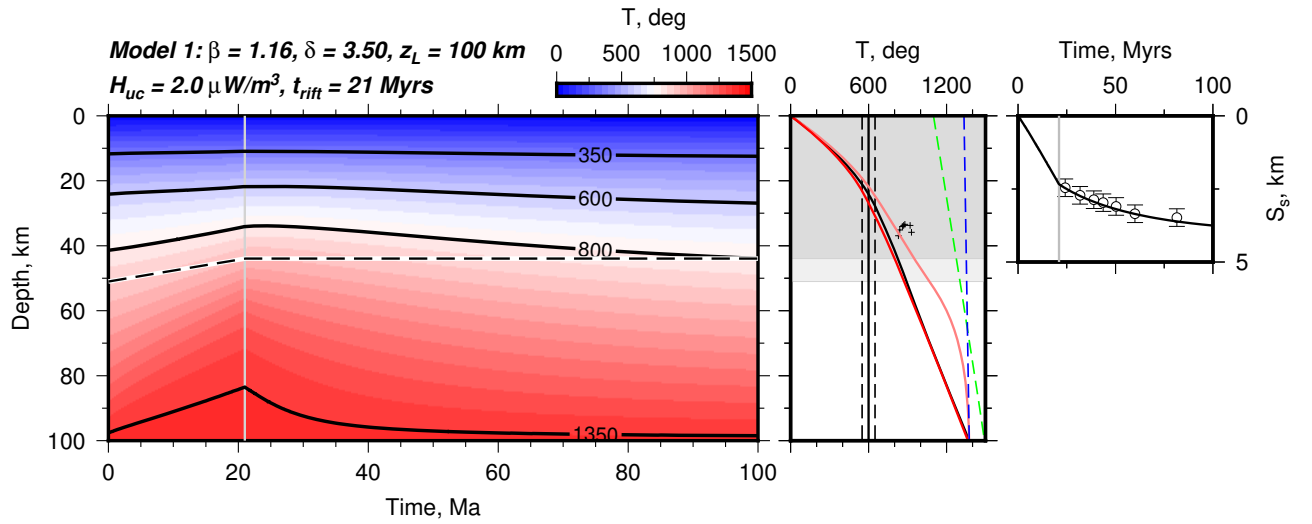
$$\begin{aligned} 30 \leq z_c \leq 45 \quad \text{km} \quad \text{at} \quad t = 0 \quad \text{Myrs} \\ 100 \leq z_l \leq 150 \quad \text{km} \quad \text{at} \quad t = 0 \quad \text{Myrs}, \end{aligned} \quad (10)$$

where  $z_l$  is the thickness of the lithosphere and  $t = 0$  is the present day.

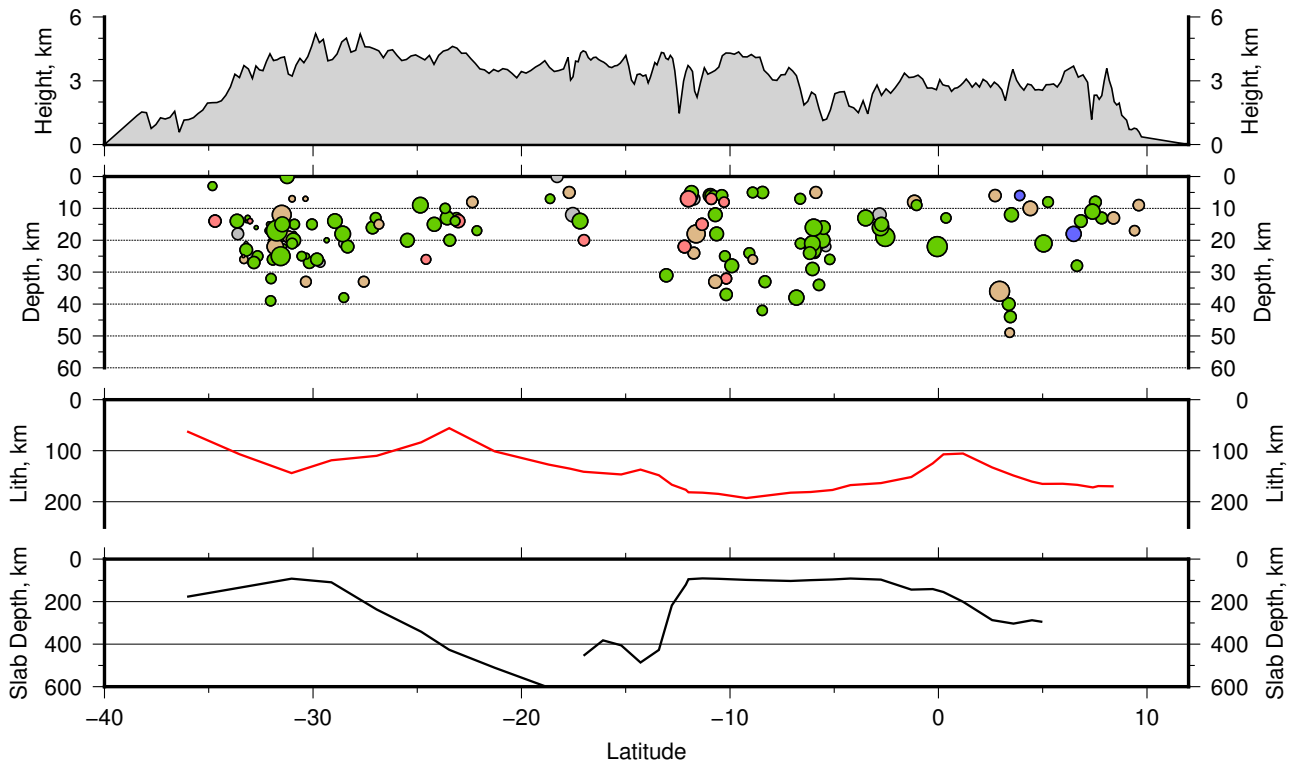
In order to explore the range of models that fit these constraints, I performed a grid-search over a range of the key material and geometrical parameters that influence both the temperature structure and subsidence history within the rift. The parameters were randomly selected from a pre-defined range (equivalent to using uniform priors), with the parameter range given in Supplementary Table 2.

Parameter	Symbol	Range
Initial lithosphere thickness	$z_l$	75–150 km
Initial crustal thickness	$z_c$	40–60 km
Upper crust thickness	$z_{uc}$	10–30 km
Crustal stretching factor	$\beta$	1.05–1.4
Mantle stretching factor	$\delta$	1.0–6.0
Rift duration	$t_{rift}$	10–30 Myrs
Upper crustal radiogenic heating	$H_{uc}$	1.0–2.5 $\mu\text{W}/\text{m}^2$
Lower crustal radiogenic heating	$H_{lc}$	0.2–0.8 $\mu\text{W}/\text{m}^2$

**Supplementary Table 2:** Parameter range explored in the rifting models.

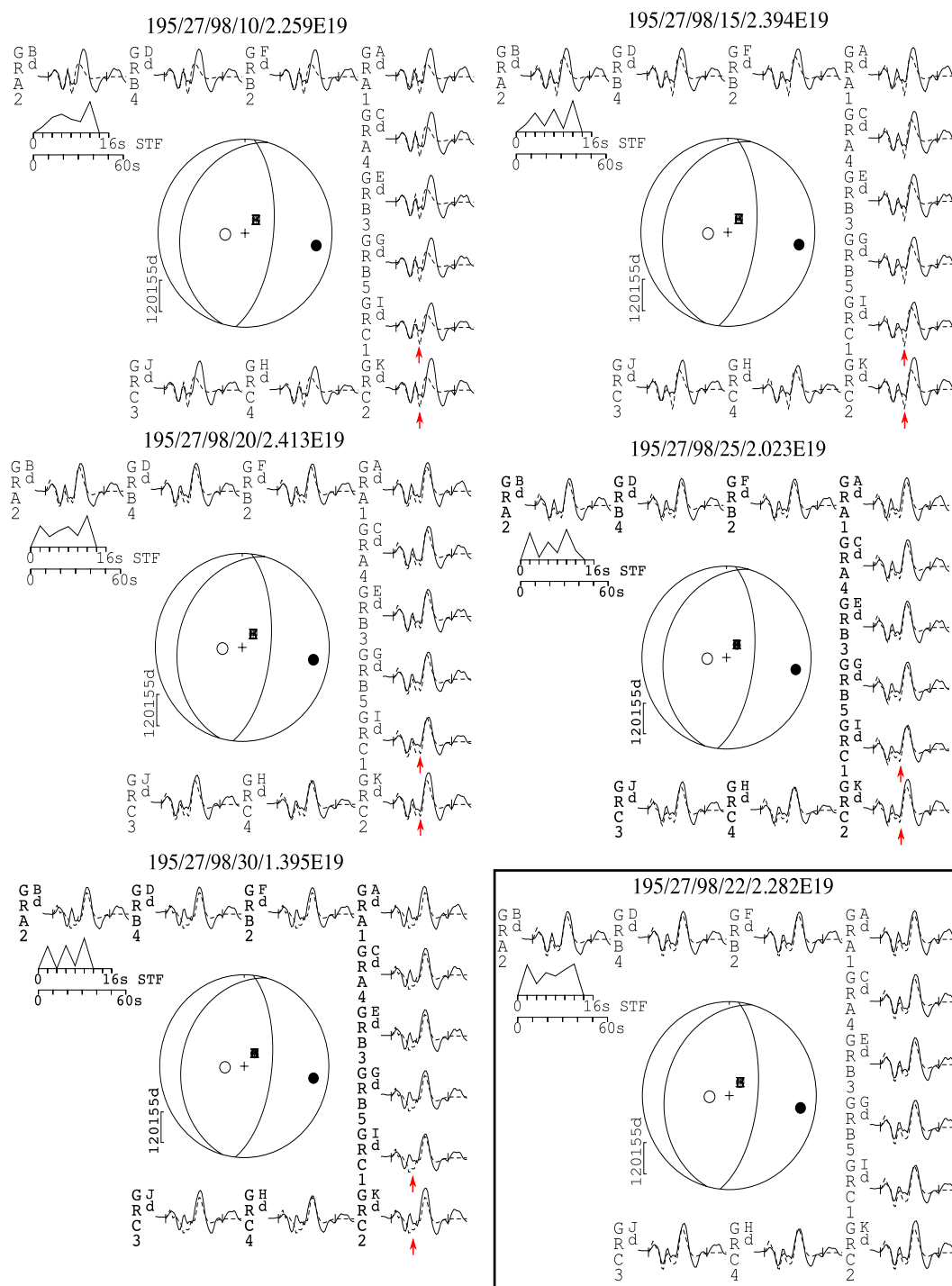


**Supplementary Figure 2:** Temperature evolution for one of the best-fitting rift models. The left-hand panel shows the temperature-time evolution, overlain by the 350, 600, 800 and 1350°C contours. The black-dashed line is the Moho through time. The middle panel shows the 1-D pre-rift (black), syn-rift (light red) and end-rift (red) geotherms. The green dashed line is the peridotite solidus, and the blue dashed line is the mantle isentrope. The vertical black solid line demonstrates where the geotherm crosses the 600°C isotherm (~30 km). The light grey and dark grey areas are the pre- and post-rift crustal thickness, respectively. The right-hand panel shows the modelled (black line) and the observed (white circles) sediment-loaded subsidence through time.

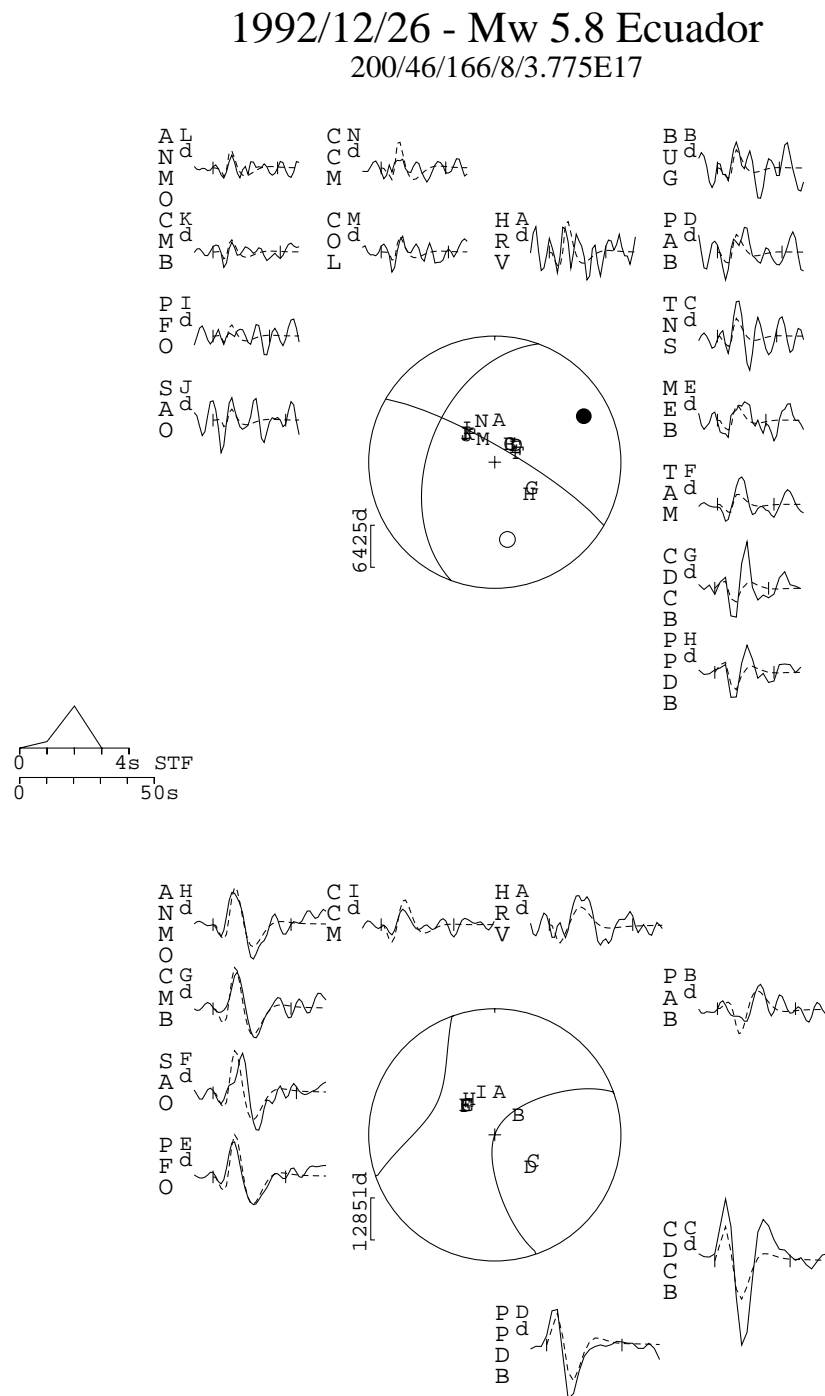
172 **Text S3: Seismicity, Slab Depth and Lithosphere Thickness**

**Supplementary Figure 3:** Comparison between the topography, earthquake centroid depths, lithosphere thickness in the forelands [Priestley and McKenzie, 2013] and the depth of the surface of the Nazca plate from Slab 2.0 [Hayes et al., 2018]. Lithospheric thickness is unlikely to be particularly well resolved in regions where the Nazca plate is shallow, because fast  $V_s$  anomalies associated with the plate will be smeared horizontally over the  $\sim 300$  km resolution of the tomographic model into the forelands, potentially biasing the lithosphere thickness estimates to being too high. This is clear from the anti-correlation between the Nazca plate depth and the lithosphere thickness beneath the forelands (i.e. lithosphere thickness is largest where the Nazca Slab depth is the shallowest).

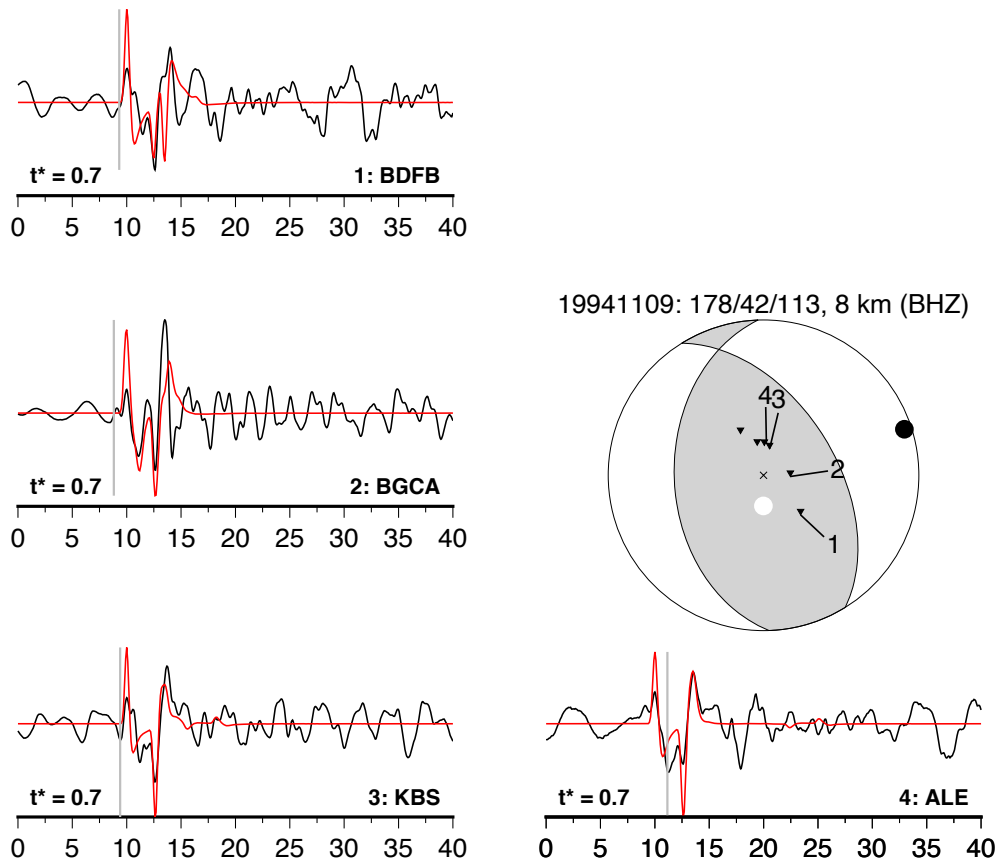
## 1987/03/06 - Mw 7.0 Ecuador



**Supplementary Figure 4:** Depth sensitivity tests for the 6th March 1987 earthquake in Ecuador. Only a small number of co-located, vertical-component stations were available for this event, but these provide a reasonable constraint on the earthquake depth. I fixed the earthquake mechanism to the gCMT best double-couple solution and performed inversions where the source-time function was able to vary but the depth was fixed to values between 10 km and 30 km. Small red arrows point to the key phase that constrains the event depth to be  $\sim 20$ -25 km. The minimum misfit model is shown on the bottom right.

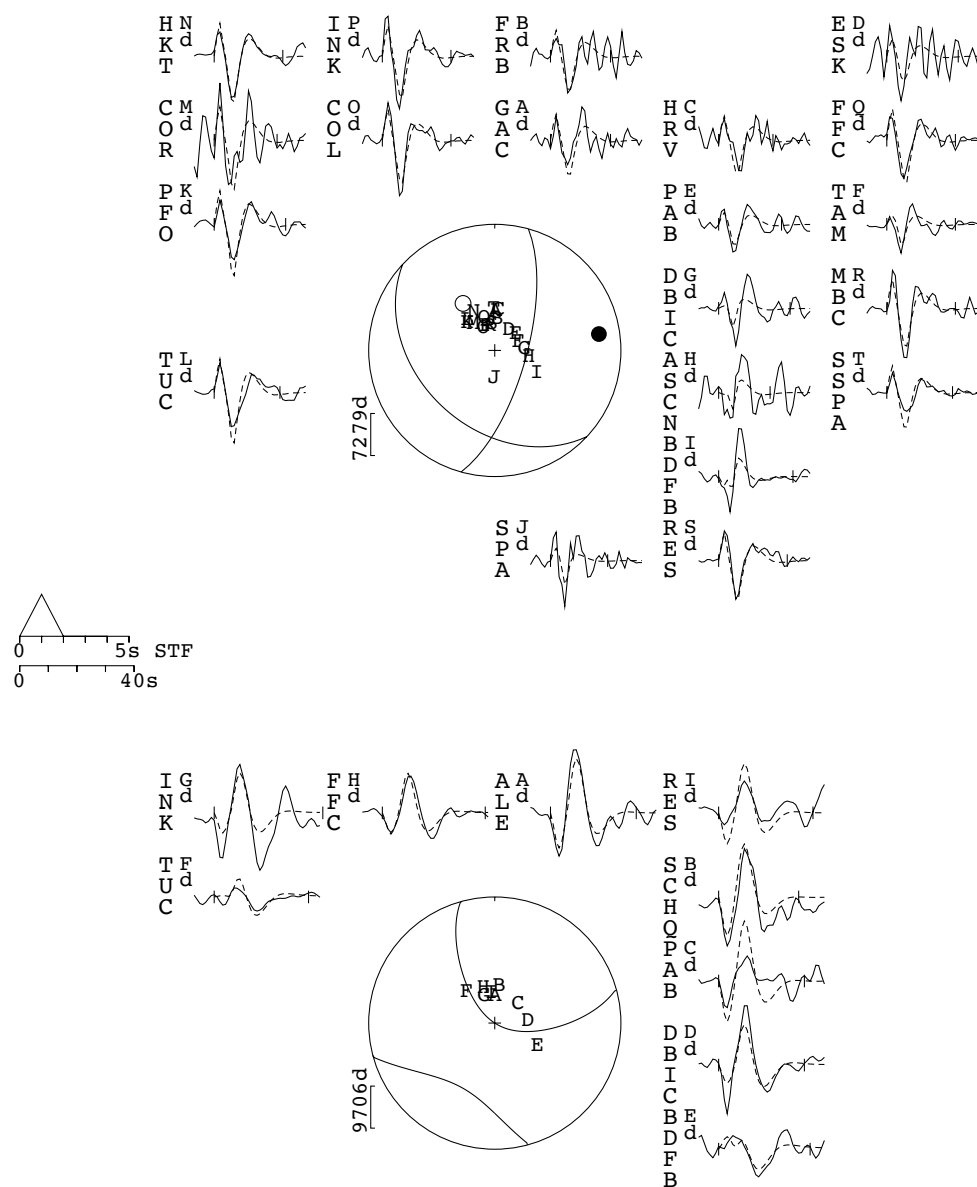


**Supplementary Figure 5:** Minimum-misfit teleseismic body-waveform model for the 26th December 1992 earthquake in Ecuador. The strike, dip, rake, centroid depth and moment release in Newton metres are shown beneath the title. The observed (solid) and modelled (dashed) vertical-component seismograms are shown at the top around the  $P$ -wave focal mechanism, and the transverse-component seismograms are shown at the bottom. The four/three-letter station code is shown to the left of each seismogram. The source-time function (STF) is shown by the triangles in the centre of the figure. All other figures of long-period body-waveform modelling results follow this same format.



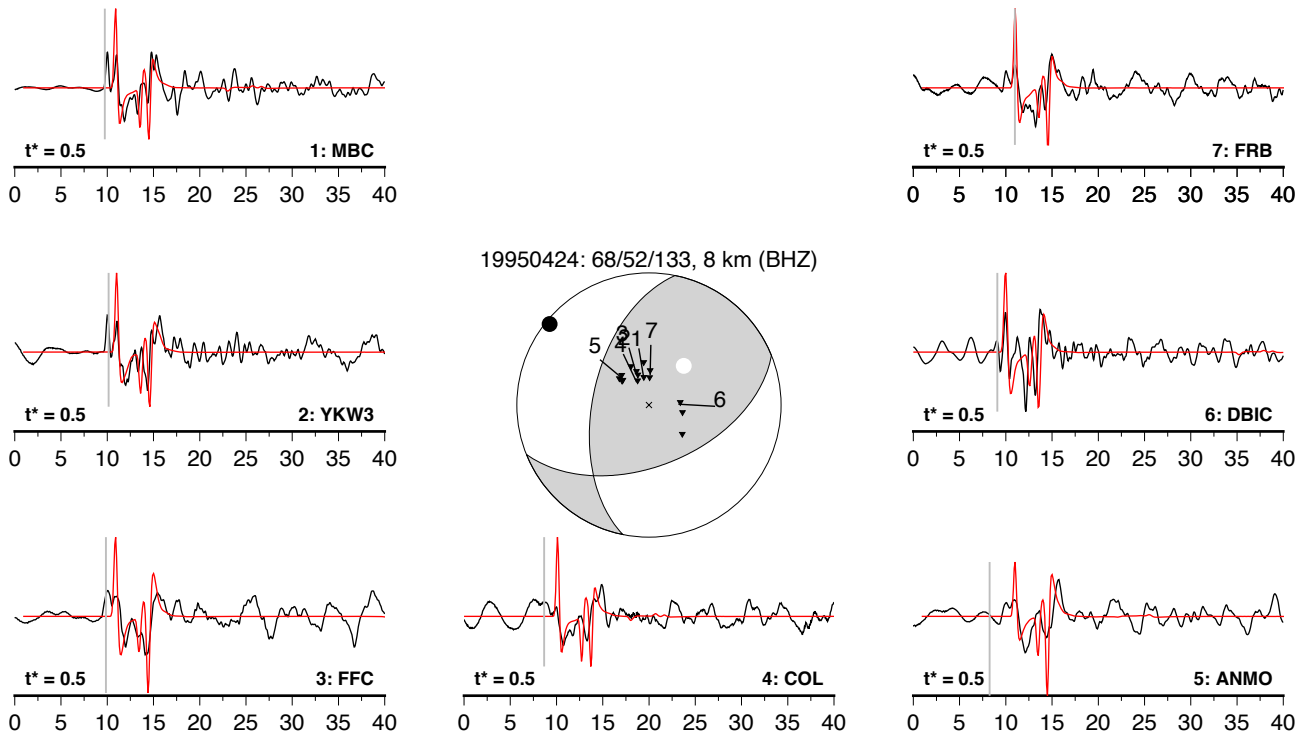
**Supplementary Figure 6:** Broadband vertical-component seismograms (black) and synthetics (red) for the 9th November 1994 earthquake. The strike, dip, rake and centroid depth are shown above the focal mechanism. Black triangles in the focal mechanism mark stations with compressional  $P$ -wave arrivals, and light-grey triangles mark stations with dilatational  $P$ -wave first arrivals. All other figures of broadband body-waveform modelling results follow this same format.

1995/10/07 - Mw 5.8 Ecuador  
133/39/34/12/3.315E17

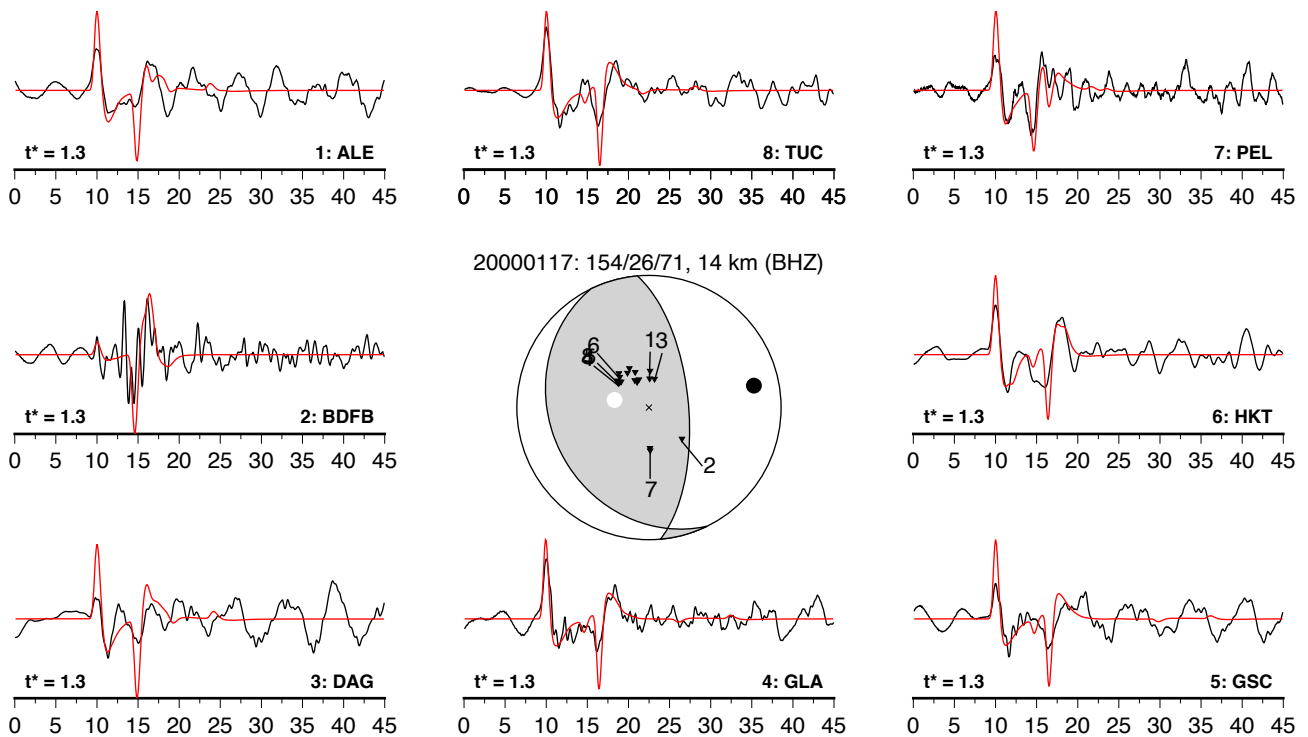


**Supplementary Figure 7:** Minimum-misfit teleseismic body-waveform model for the 7th November 1995 earthquake in Ecuador.

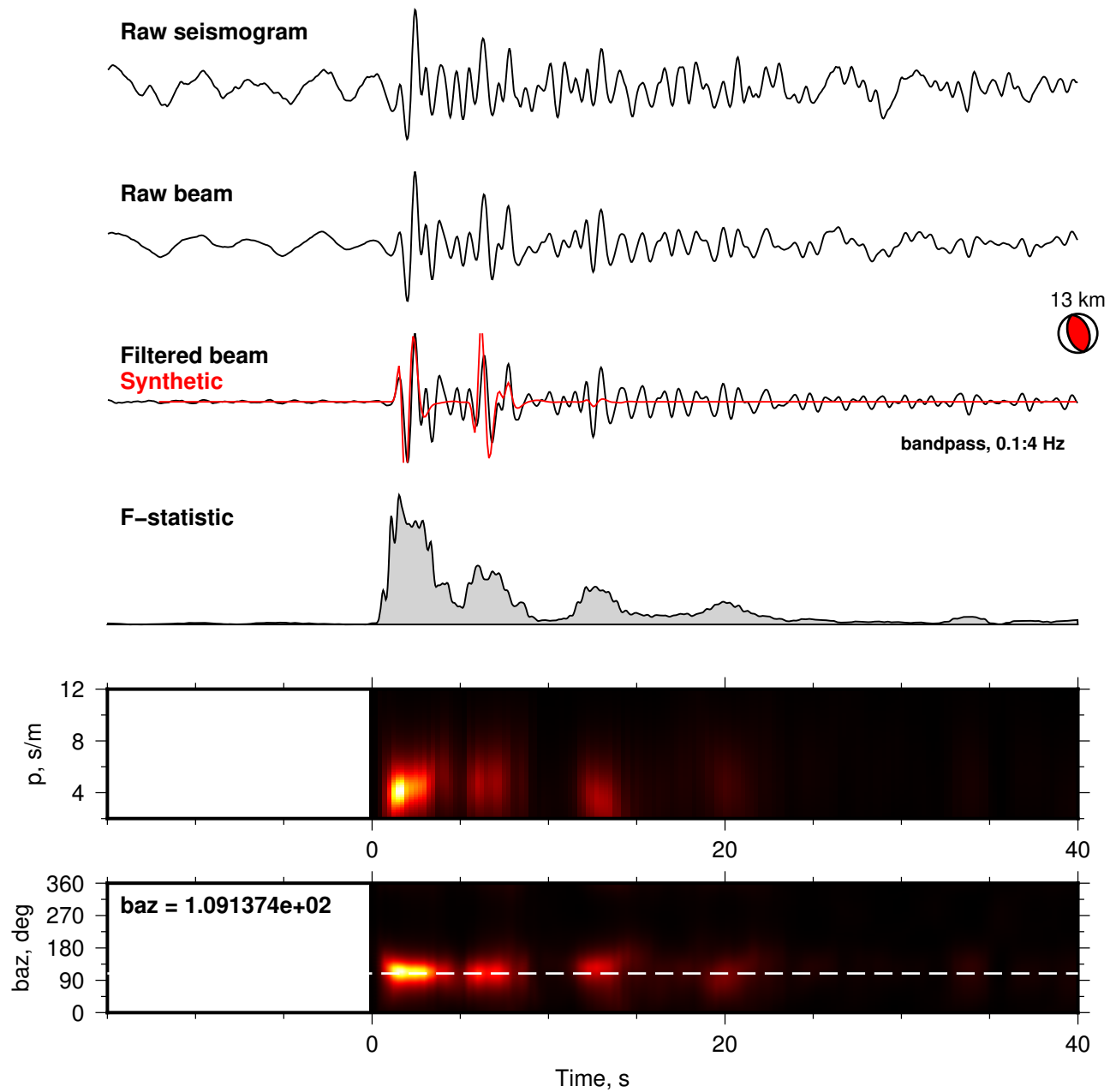




**Supplementary Figure 8:** Broadband vertical-component seismograms (black) and synthetics (red) for the 23rd April 1995 earthquake. The direct arrival has a double peak, suggesting that the source may have been more complex than the simple instantaneous rupture that I assume in the modelling. I aligned the synthetics on the second peak, but the estimated uncertainties account for mis-alignment.



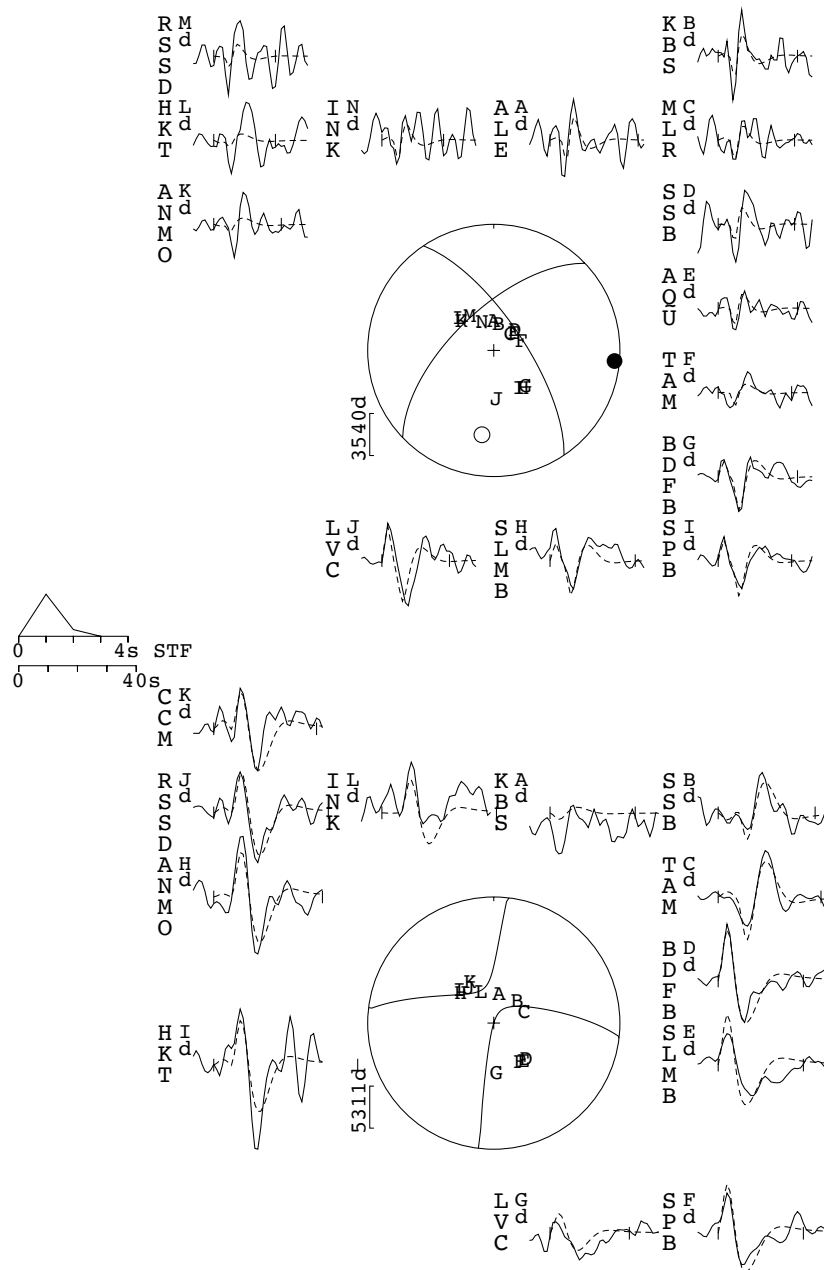
**Supplementary Figure 9:** Broadband vertical-component seismograms (black) and synthetics (red) for the 17th January 2000 earthquake.



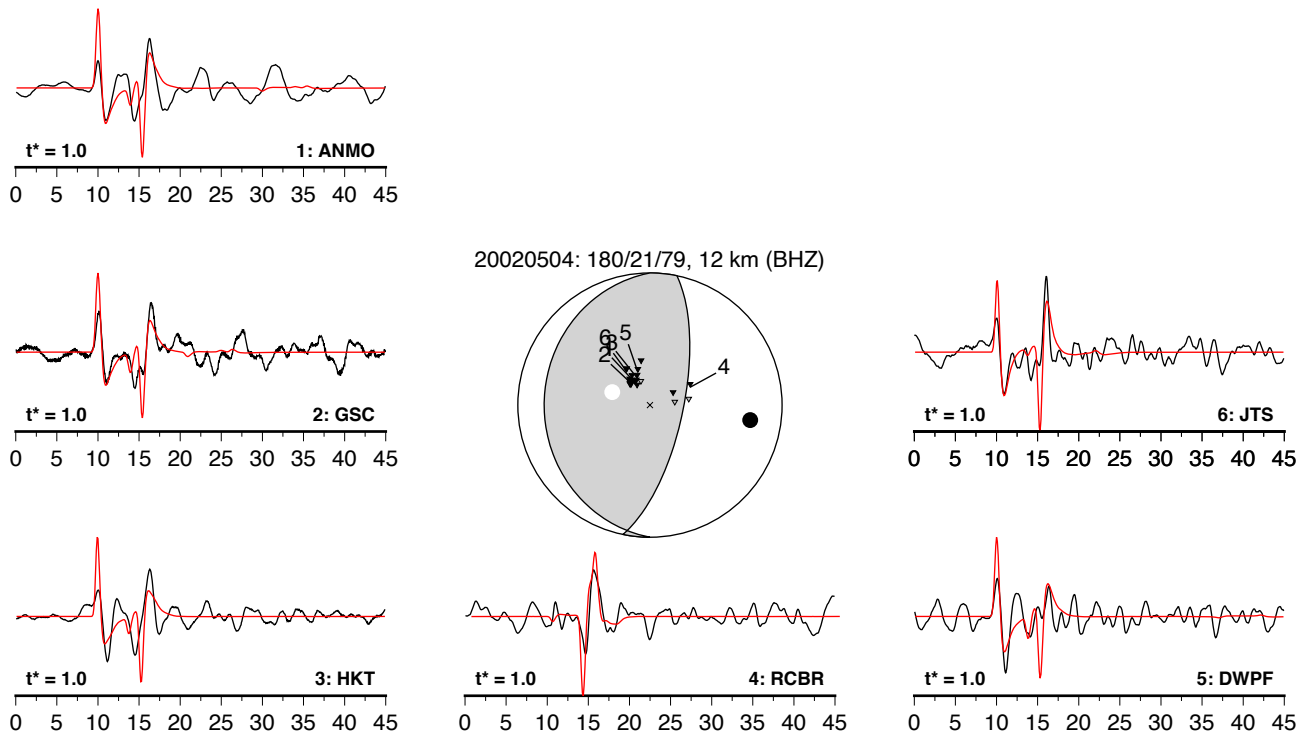
**Supplementary Figure 10:** Stacked short-period vertical-component seismograms (black) and synthetics (red) for the 8th October 2000 earthquake. Seismograms were recorded at the ILAR array. The F-statistic was calculated using the method of Heyburn and Bowers [2008]. The bottom two panels show the normalised amplitude of the F-statistic as a function of the ray parameter and back azimuth assumed in the stacking. The white dashed line shows the true back azimuth of the earthquake epicentre, highlighting that the energy arriving  $\sim 6$  s after the direct  $P$ -wave is coming from a back azimuth as the earthquake source.

# 2001/12/21 - Mw 5.6 Venezuela

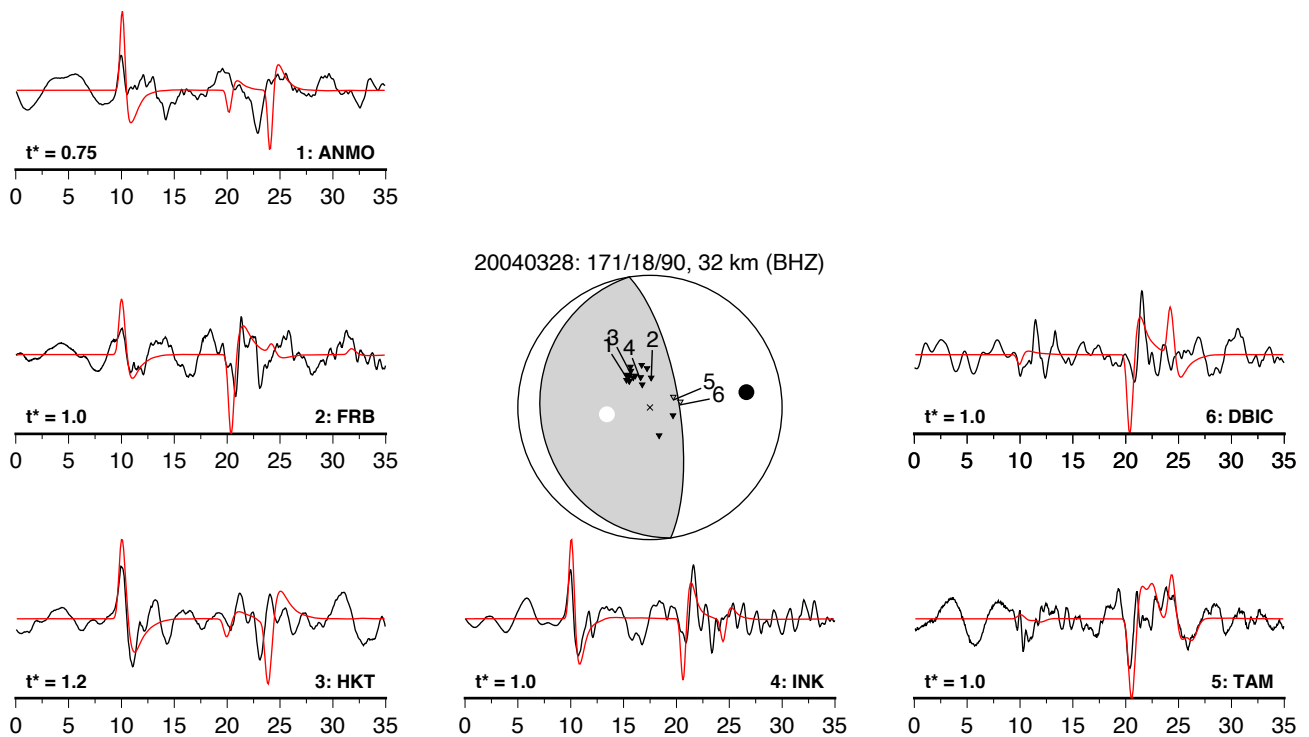
226/64/158/13/2.274E17



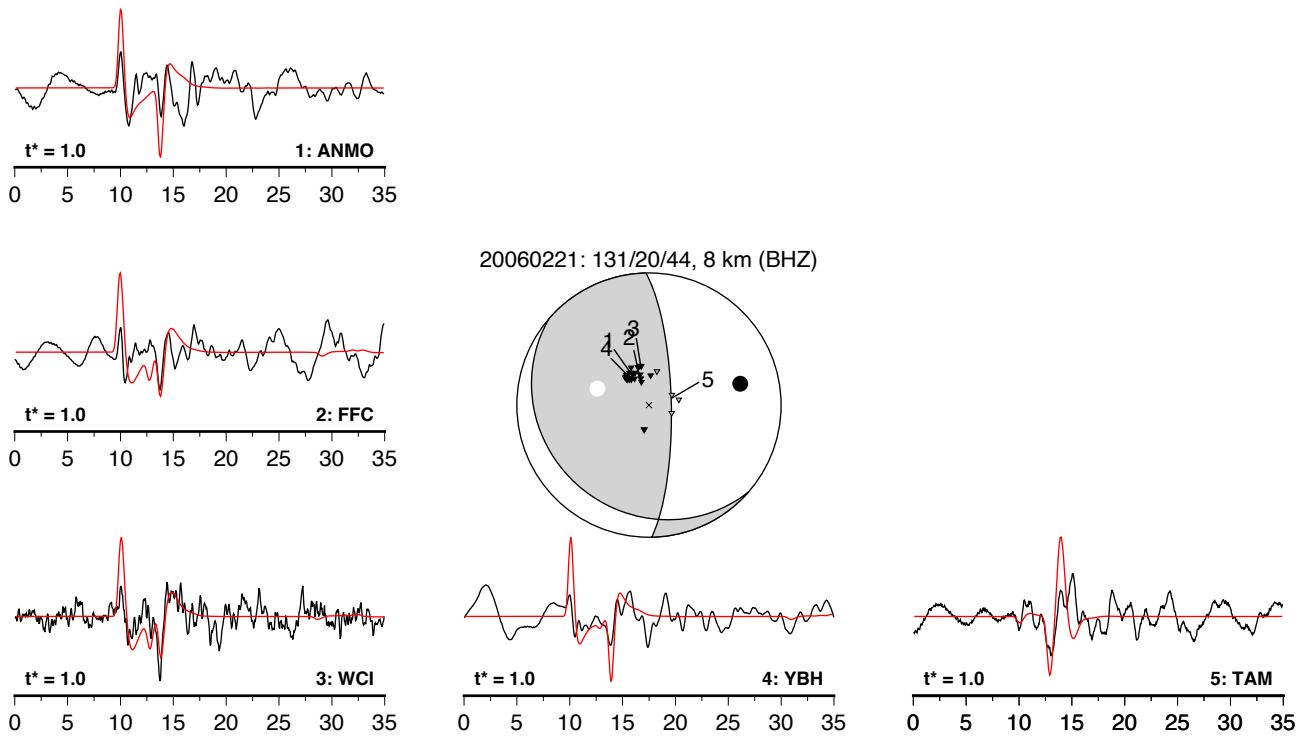
**Supplementary Figure 11:** Minimum-misfit teleseismic body-waveform model for the 21st December 2001 earthquake.



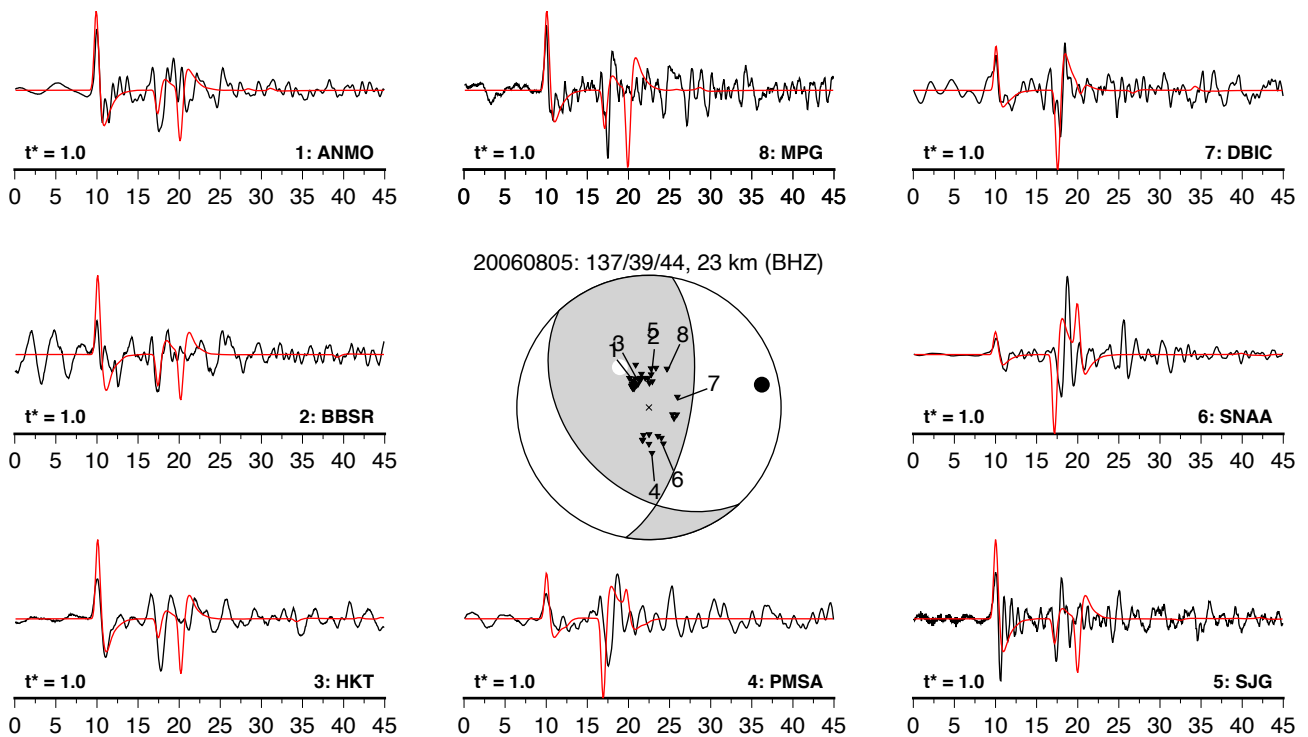
**Supplementary Figure 12:** Broadband vertical-component seismograms (black) and synthetics (red) for the 4th May 2002 earthquake.



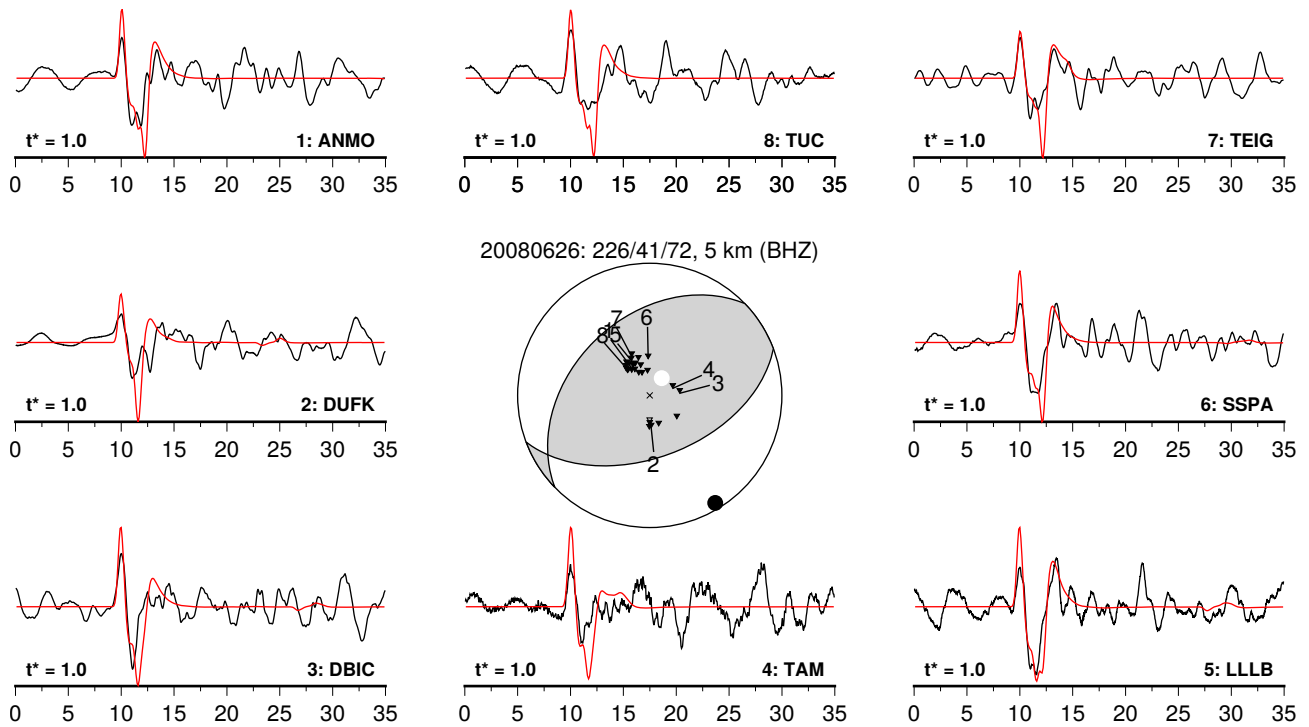
**Supplementary Figure 13:** Broadband vertical-component seismograms (black) and synthetics (red) for the 28th March 2004 earthquake.



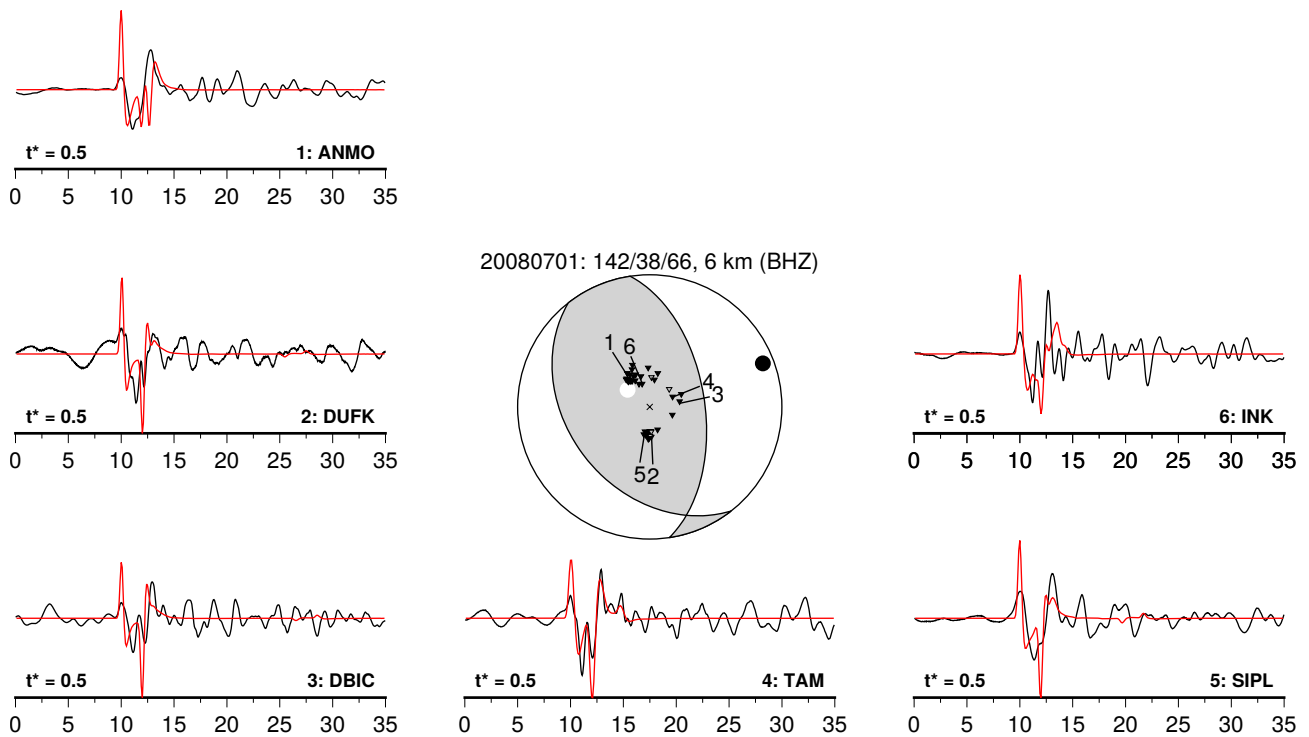
**Supplementary Figure 14:** Broadband vertical-component seismograms (black) and synthetics (red) for the 21st February 2006 earthquake.



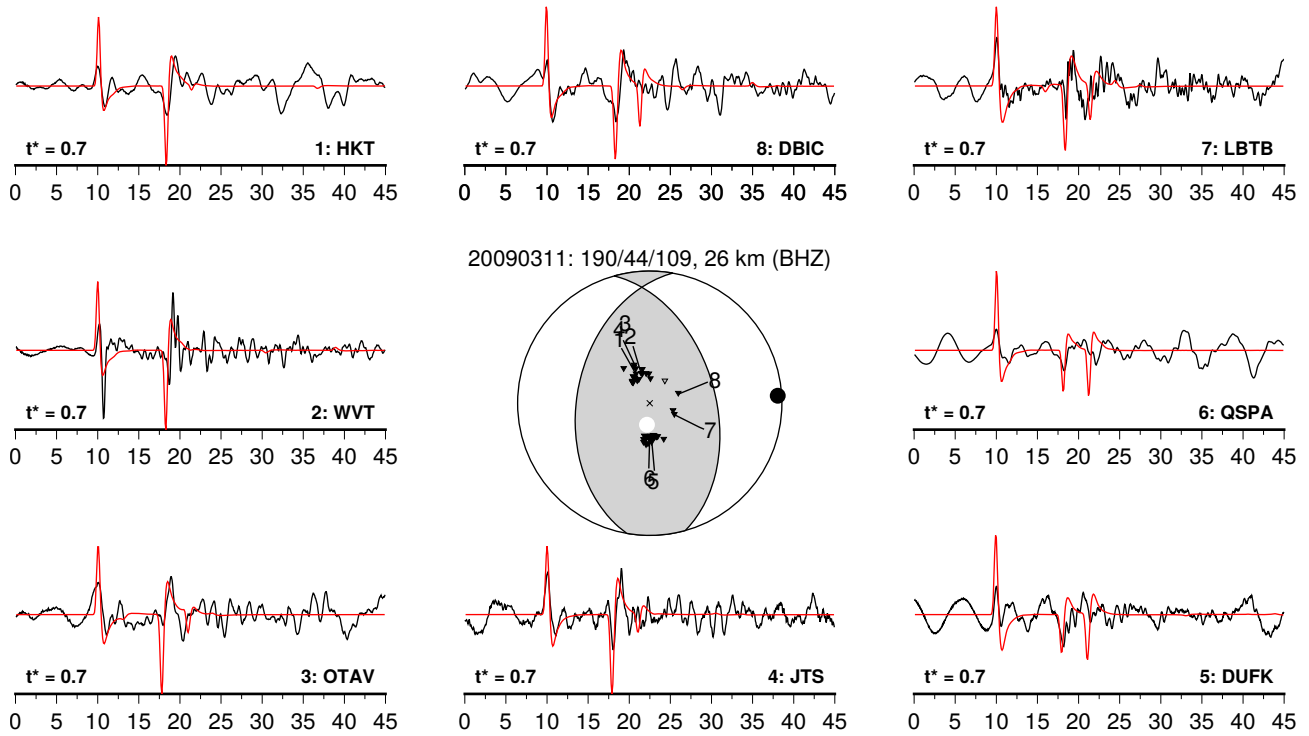
**Supplementary Figure 15:** Broadband vertical-component seismograms (black) and synthetics (red) for the 5th August 2006 earthquake.



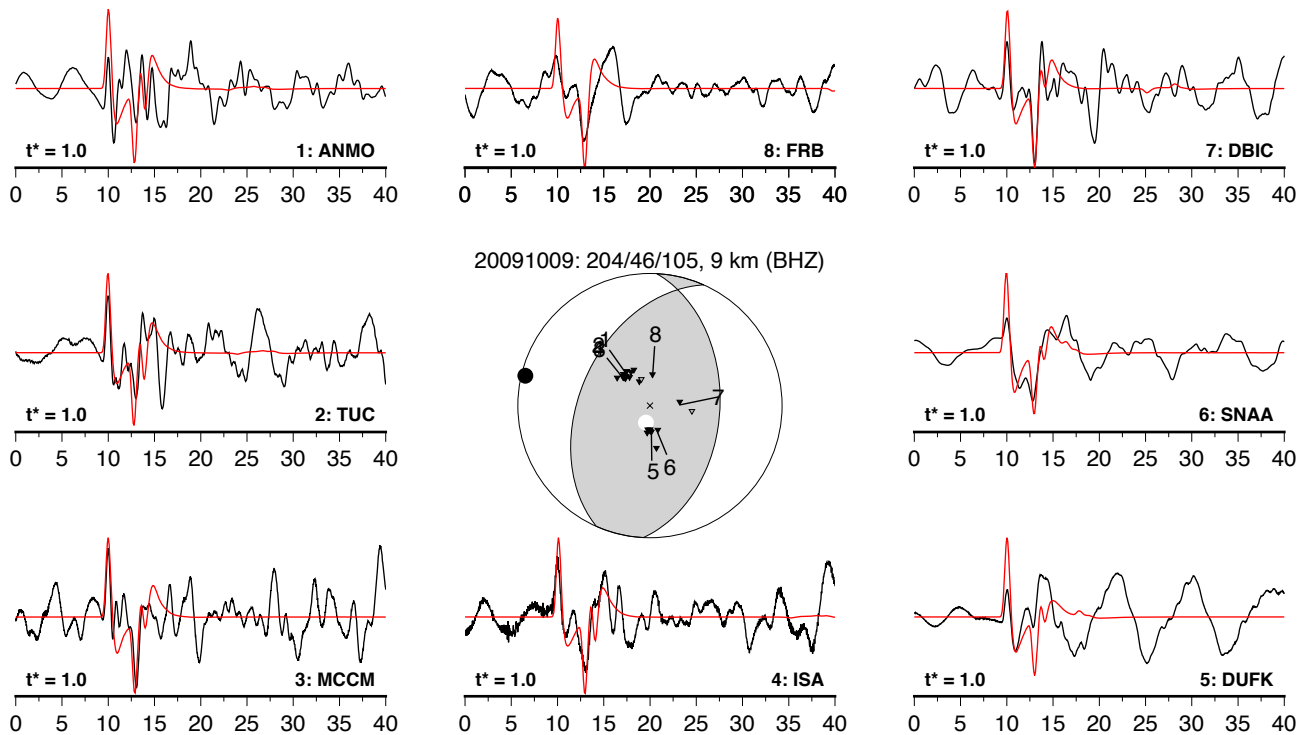
**Supplementary Figure 16:** Broadband vertical-component seismograms (black) and synthetics (red) for the 26th June 2008 earthquake.



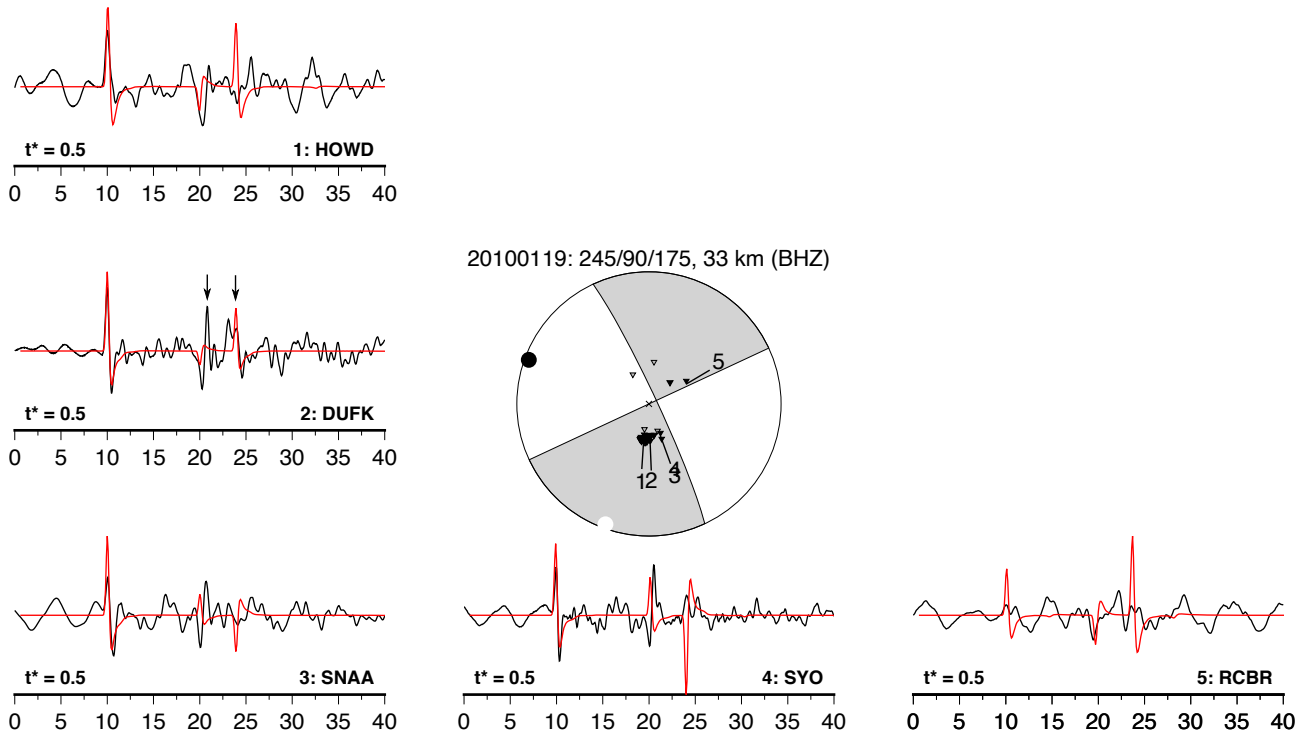
**Supplementary Figure 17:** Broadband vertical-component seismograms (black) and synthetics (red) for the 1st July 2008 earthquake.



**Supplementary Figure 18:** Broadband vertical-component seismograms (black) and synthetics (red) for the 11th March 2009 earthquake.

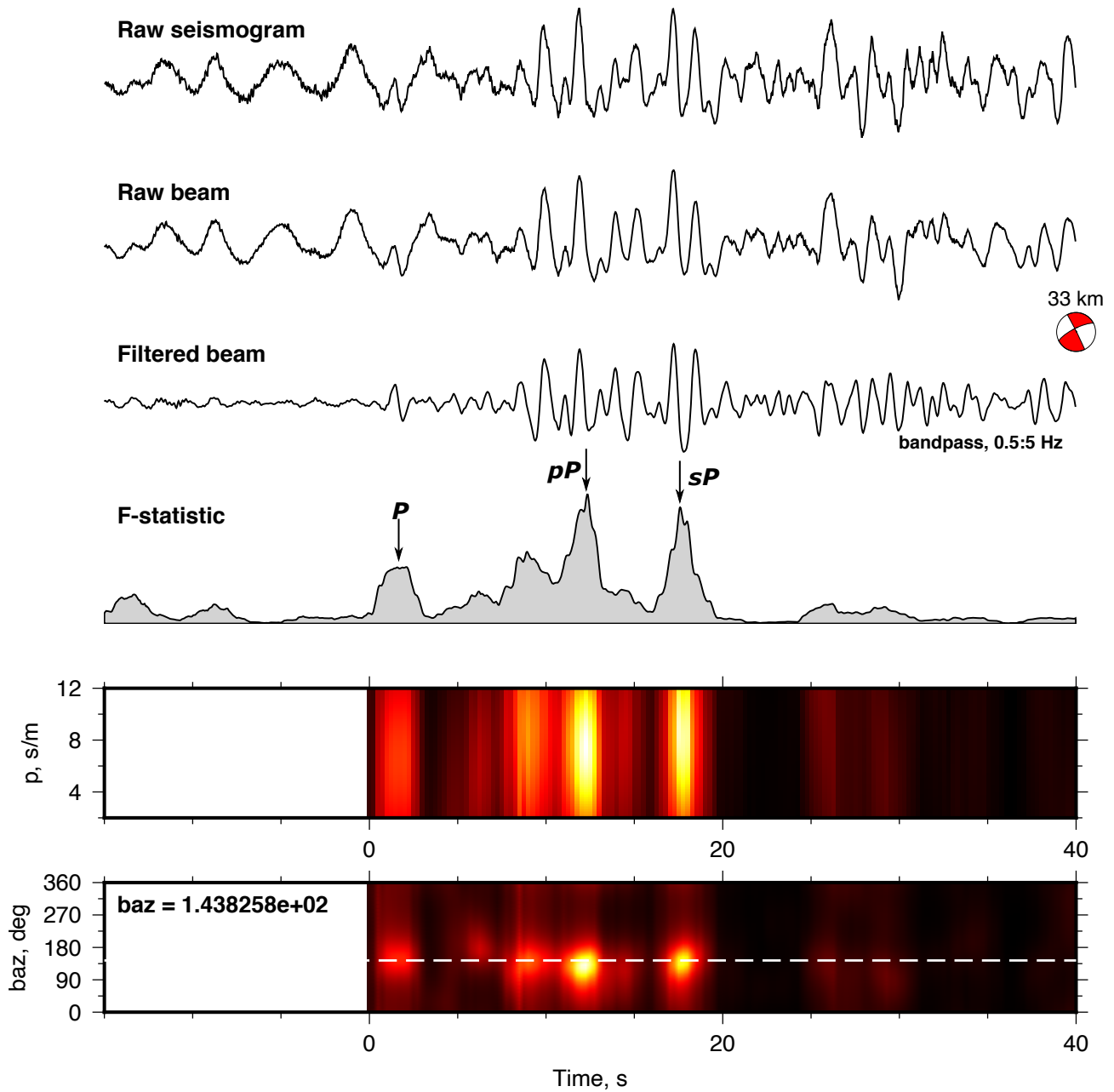


**Supplementary Figure 19:** Broadband vertical-component seismograms (black) and synthetics (red) for the 9th October 2009 earthquake.

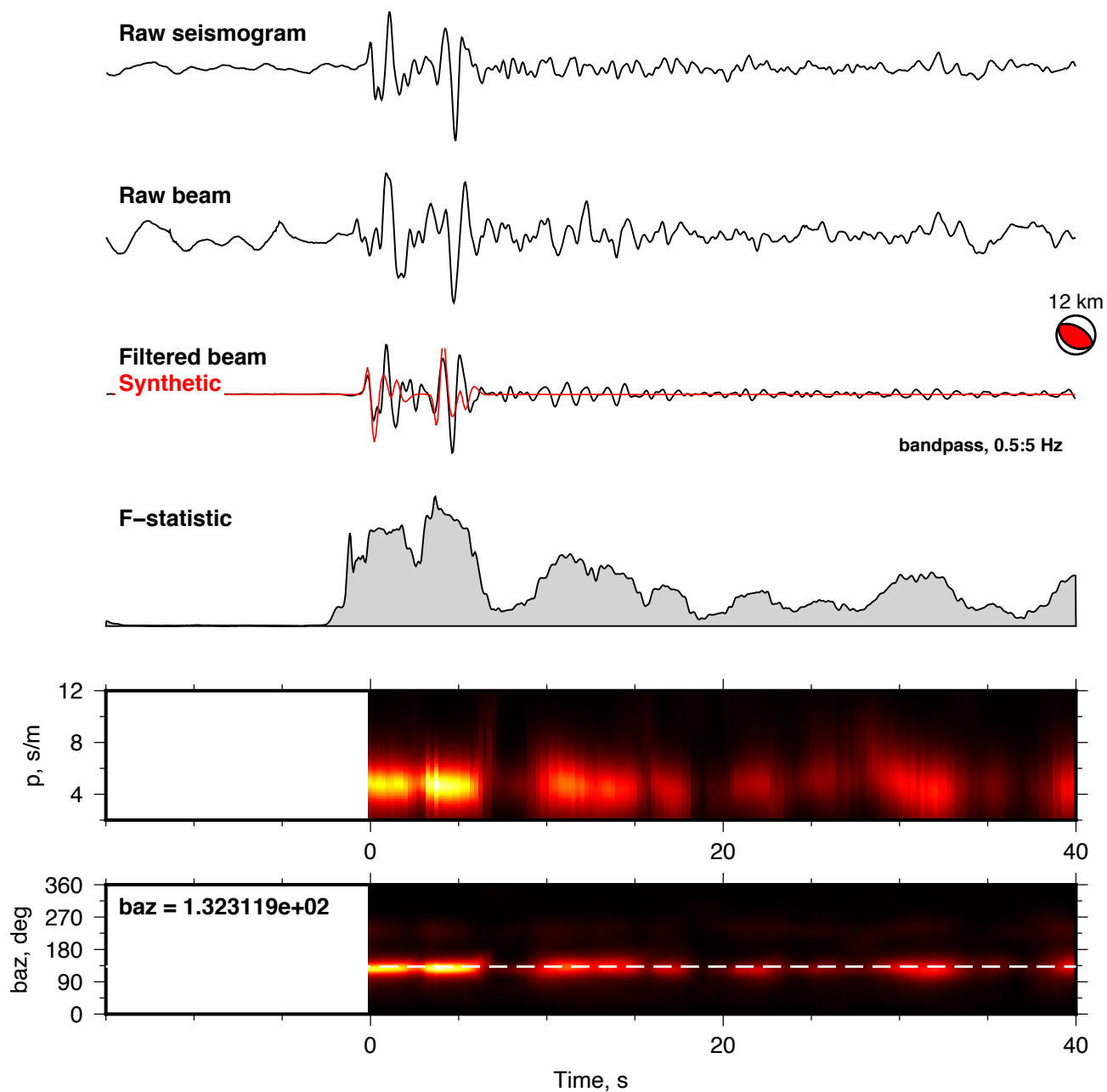


**Supplementary Figure 20:** Broadband vertical-component seismograms (black) and synthetics (red) for the 19th January 2010 earthquake. The mechanism for this event is poorly constrained and the synthetics calculated from the gCMT moment tensor predict the wrong polarity of motion for the depth phases. Nonetheless, the depths phases are clear in the *P*-wave coda as high-frequency arrivals at  $\sim 10$  and  $\sim 15$  seconds after the direct arrival and require a depth of 33 km. Beamforming the short-period seismograms from the TXAR array in North America demonstrate that these arrivals derive from a back-azimuth consistent with the earthquake epicentre (see Supplementary Figure 21).

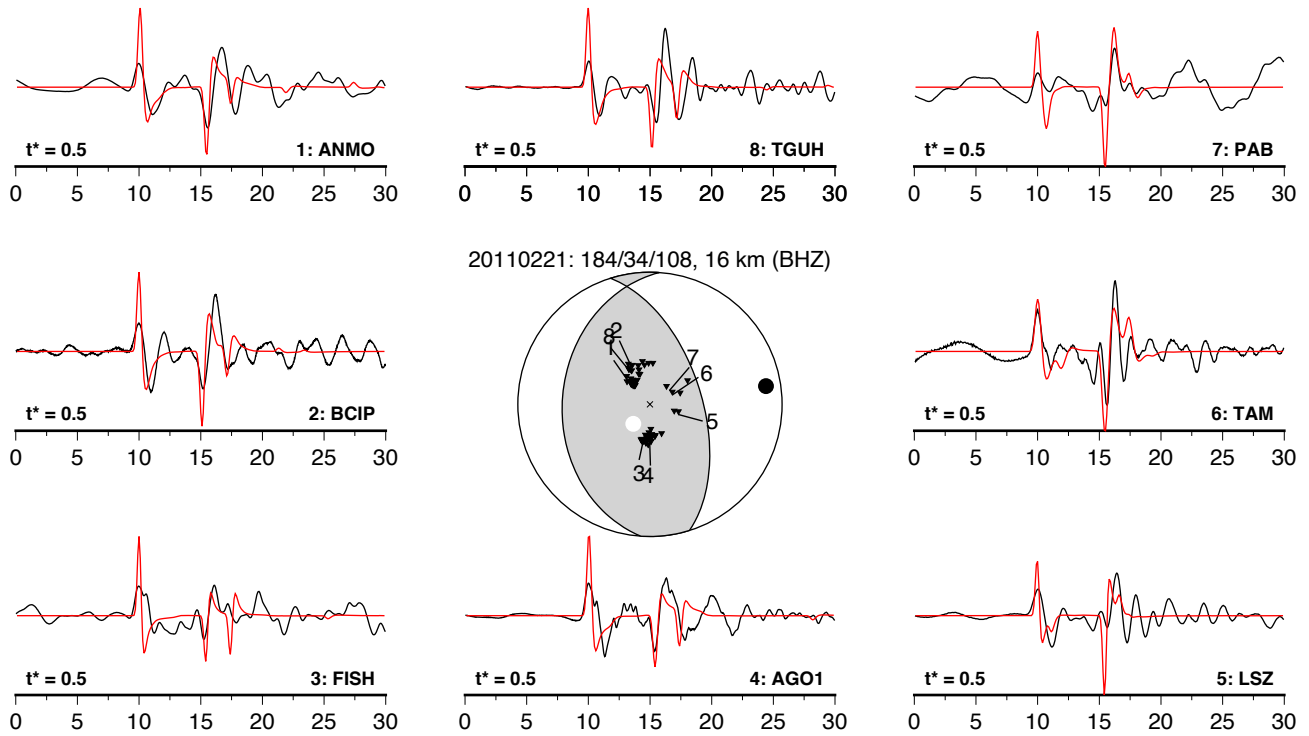




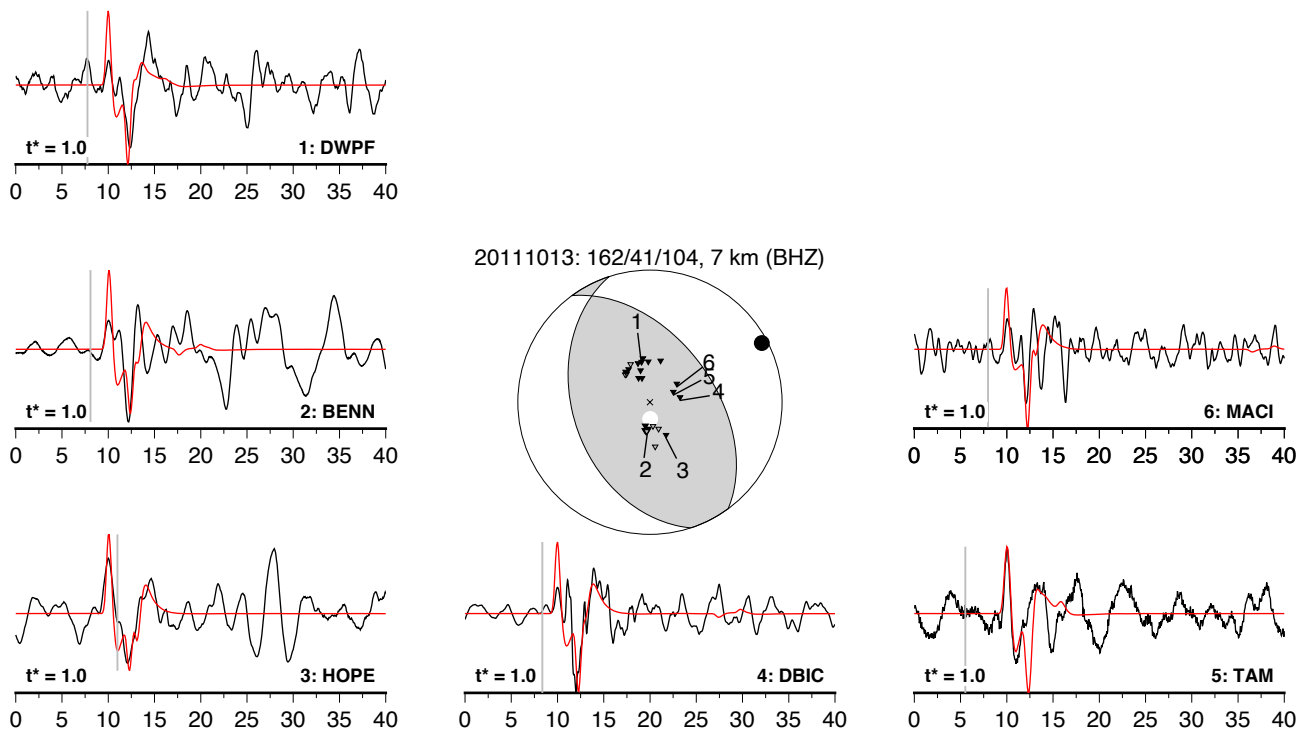
**Supplementary Figure 21:** Short-period vertical-component seismograms (black) and synthetics (red) for the 19th January 2010 earthquake. No synthetics were calculated for this event as the mechanism is poorly constrained, however the back azimuth stack demonstrates that the later arriving phases are consistent with being depth phases arriving with the same back azimuth as the direct wave.



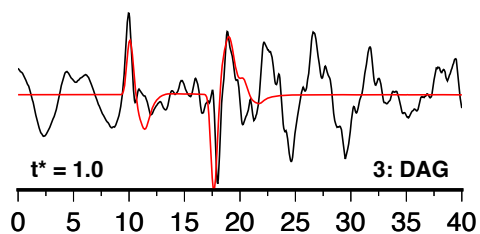
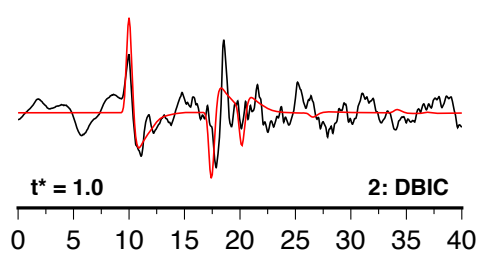
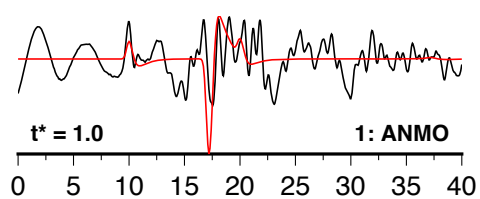
**Supplementary Figure 22:** Short-period vertical-component seismograms (black) and synthetics (red) for the 23rd January 2010 earthquake. Seismograms were recorded at the Yellowknife array.



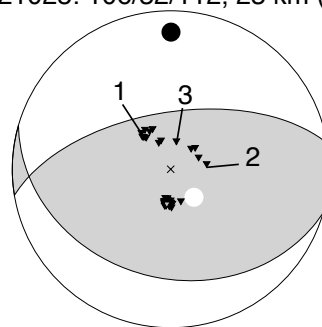
**Supplementary Figure 23:** Broadband vertical-component seismograms (black) and synthetics (red) for the 21st February 2011 earthquake.



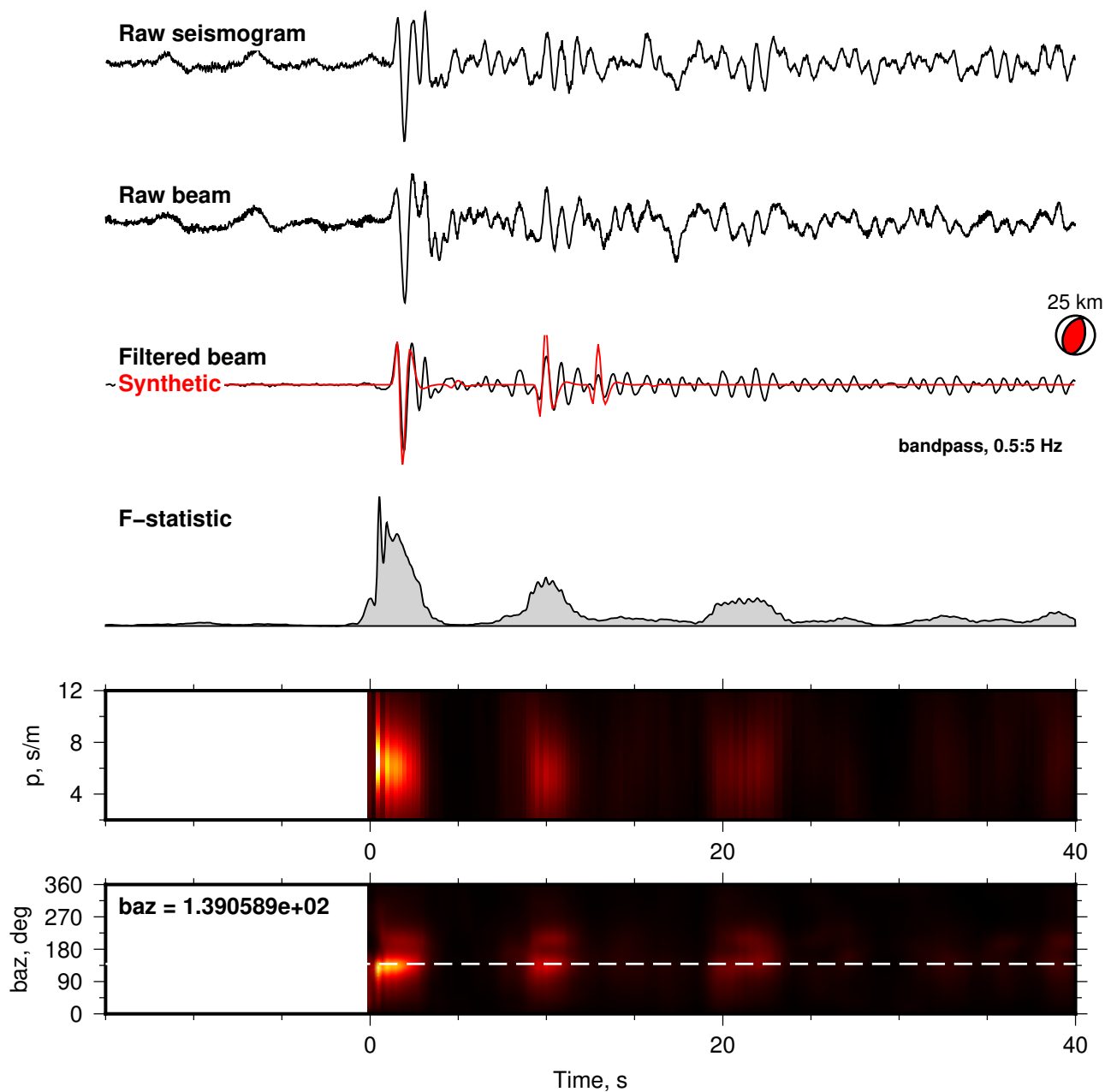
**Supplementary Figure 24:** Broadband vertical-component seismograms (black) and synthetics (red) for the 13th October 2011 earthquake.



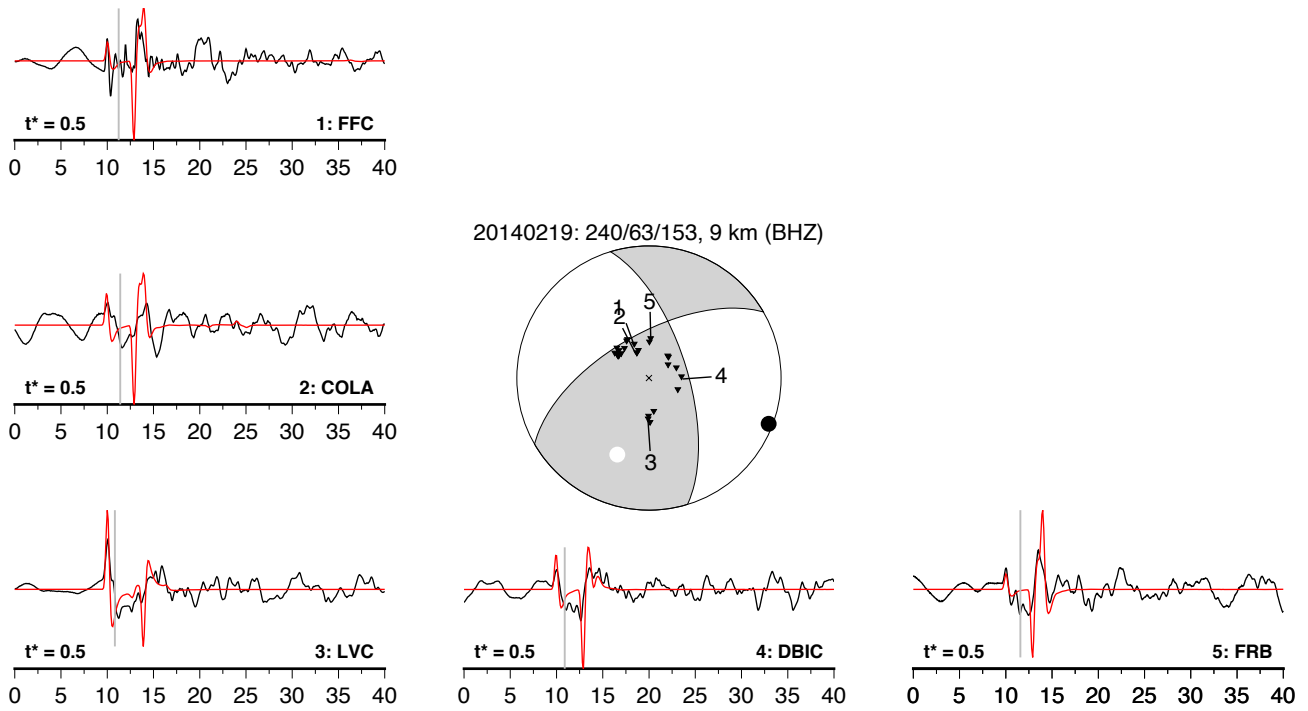
20121025: 106/32/112, 23 km (BHZ)



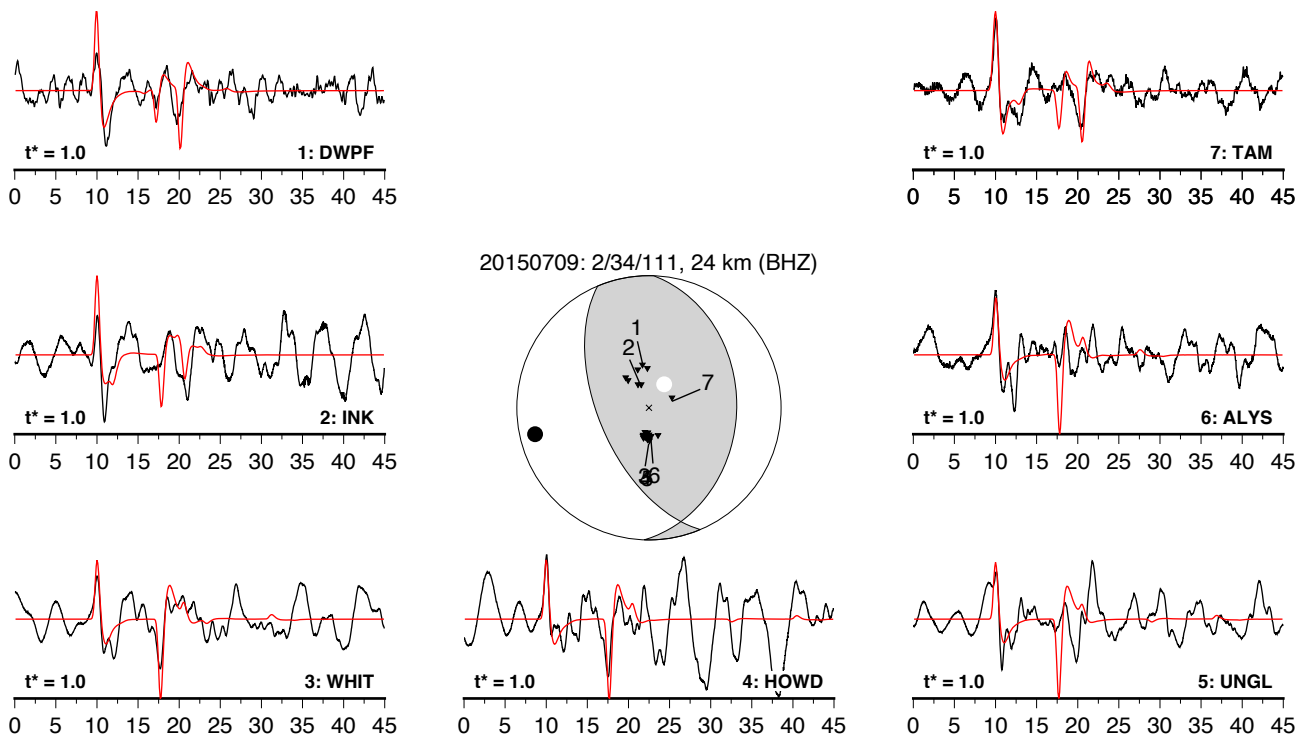
**Supplementary Figure 25:** Broadband vertical-component seismograms (black) and synthetics (red) for the 25th October 2012 earthquake.



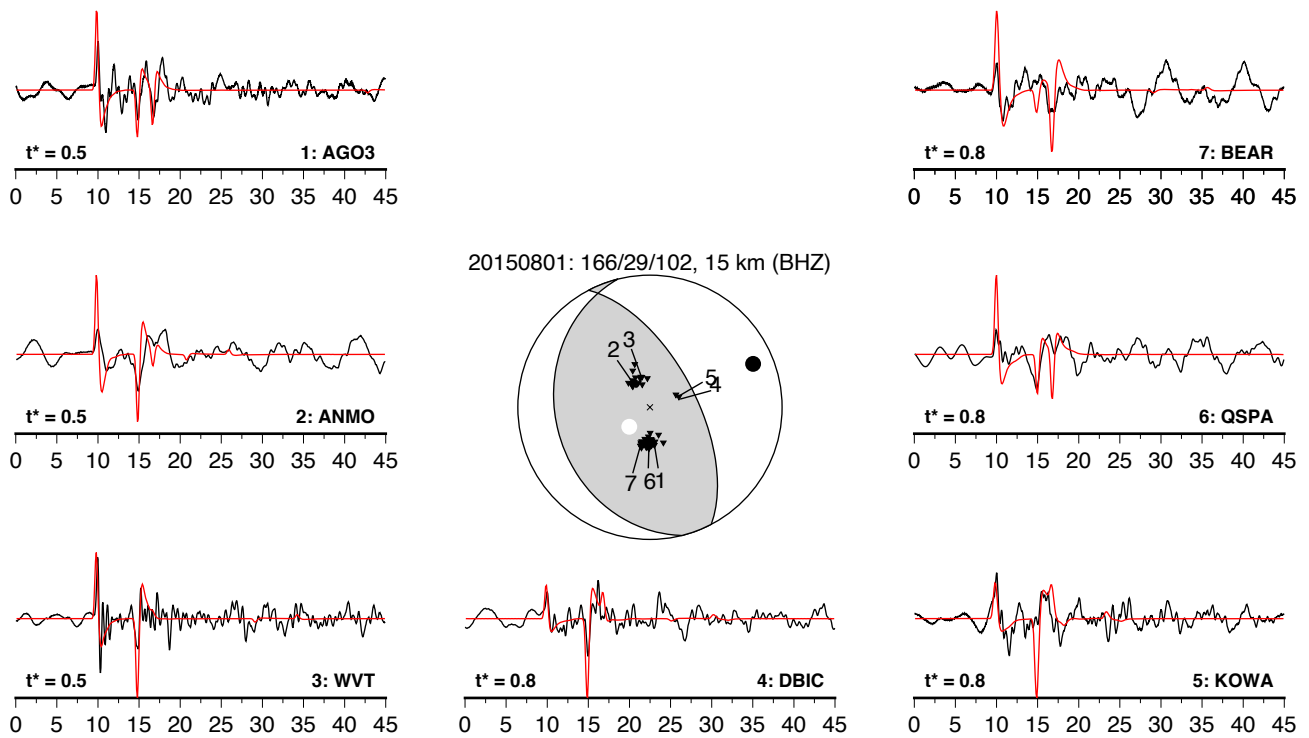
**Supplementary Figure 26:** Short-period vertical-component seismograms (black) and synthetics (red) for the 15th November 2013 earthquake. Seismograms were recorded at the NVAR array.



**Supplementary Figure 27:** Broadband vertical-component seismograms (black) and synthetics (red) for the 19th February 2014 earthquake.



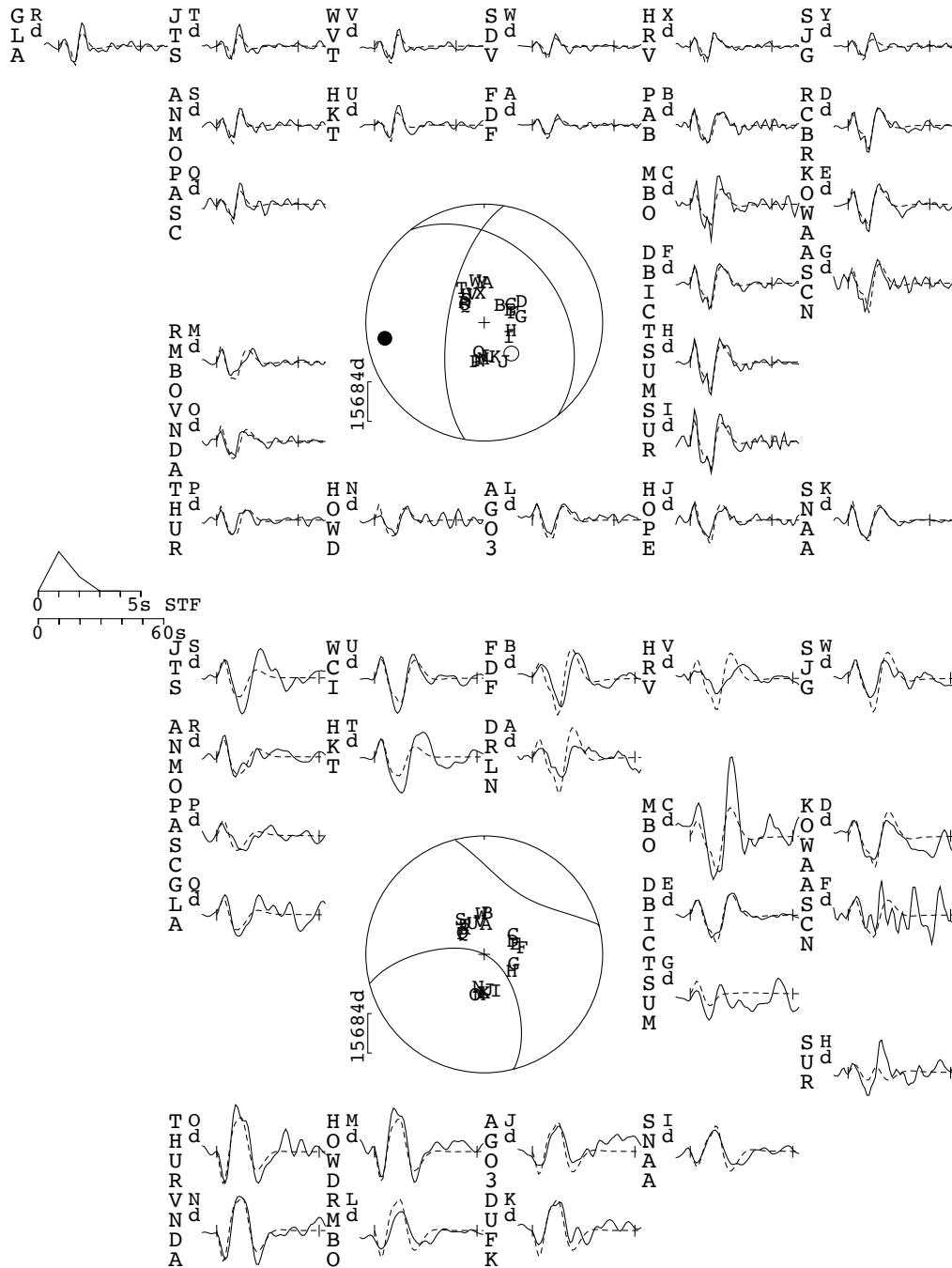
**Supplementary Figure 28:** Broadband vertical-component seismograms (black) and synthetics (red) for the 9th July 2015 earthquake.



**Supplementary Figure 29:** Broadband vertical-component seismograms (black) and synthetics (red) for the 1st August 2015 earthquake.

## 2015/10/17 - Mw 5.9 Argentina

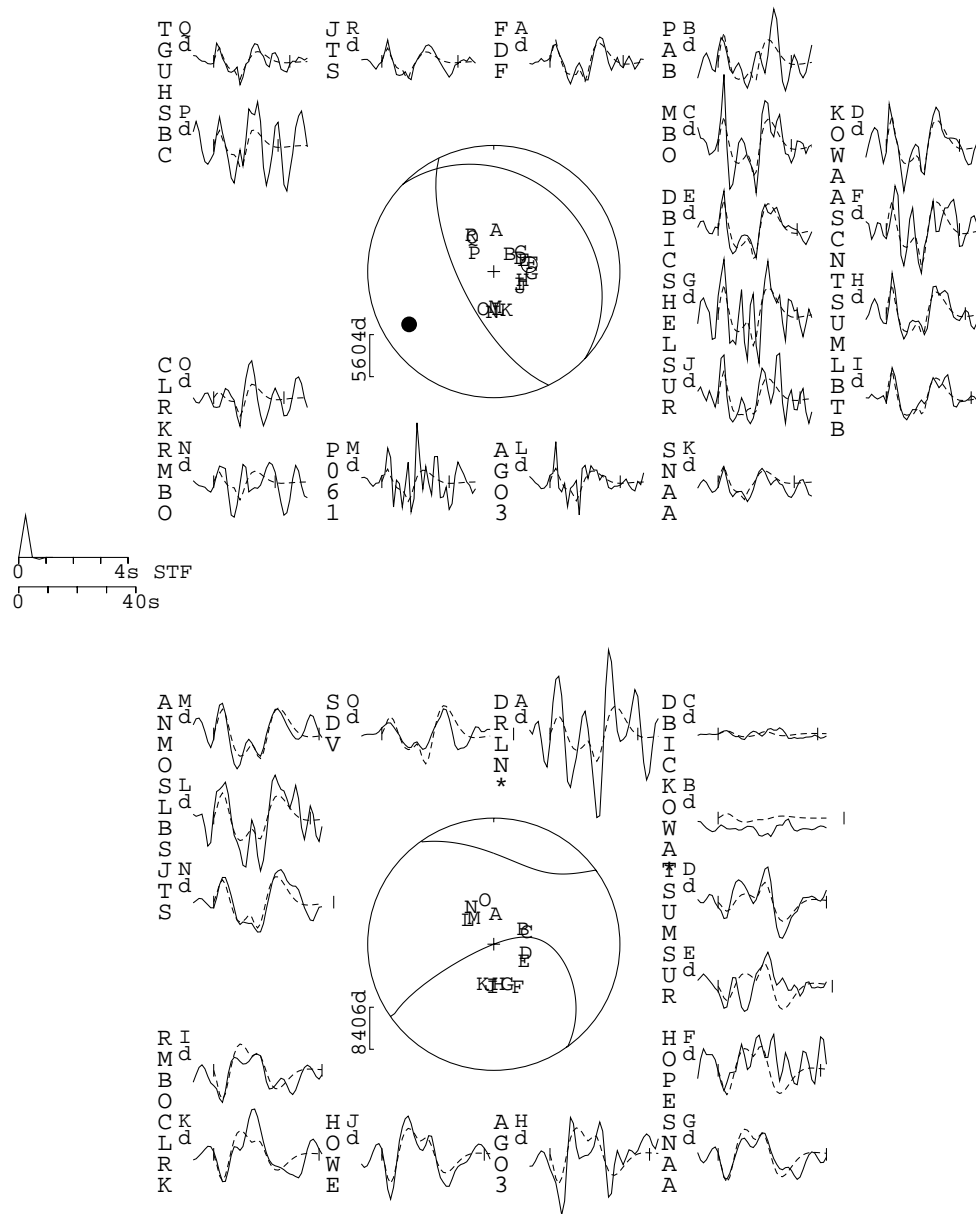
322/35/48/20/4.942E17



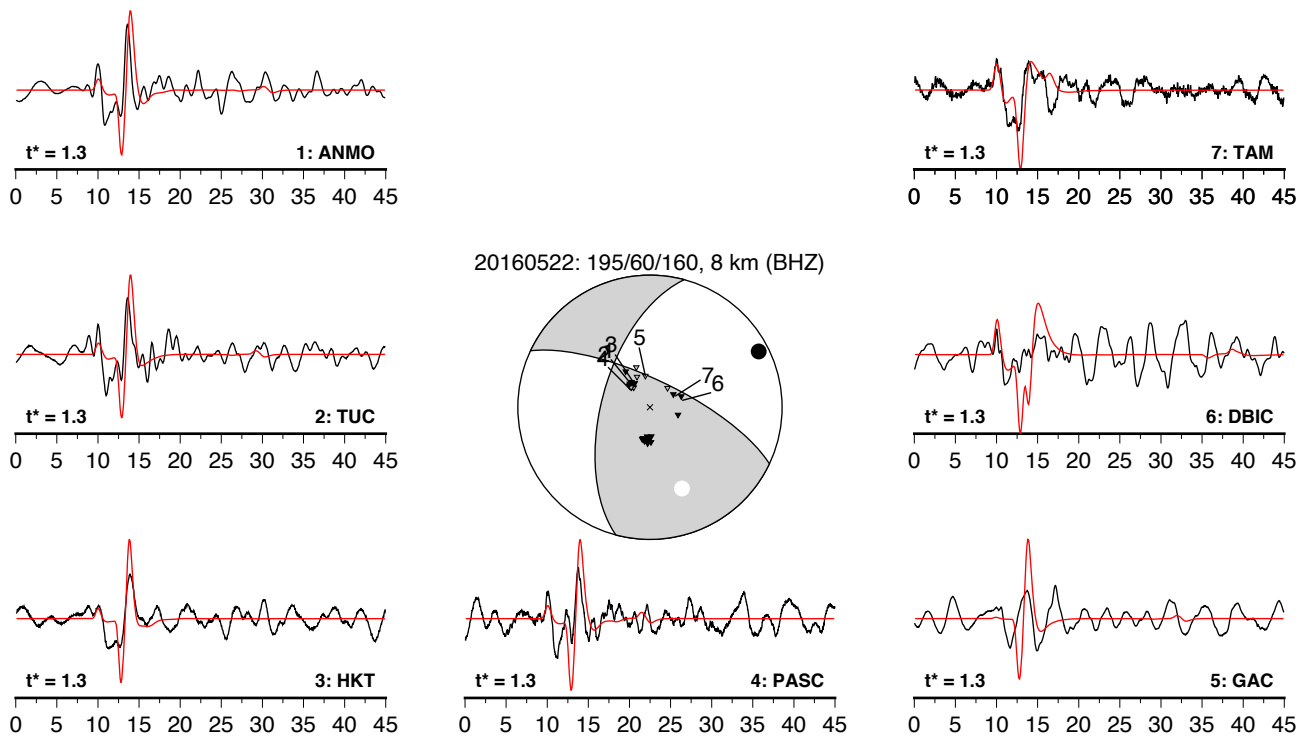
**Supplementary Figure 30:** Minimum misfit long-period teleseismic body-waveform model for the 17th October 2015 earthquake. The  $P$ - and  $SH$ -waves are relatively insensitive to the mechanism due to the station distribution, but a slight separation of the  $P$  and  $pP$ ,  $sP$  phases place good constraints on the event depth.



# 2015/11/13 - Mw 5.6 Argentina 314/24/71/26/2.089E17

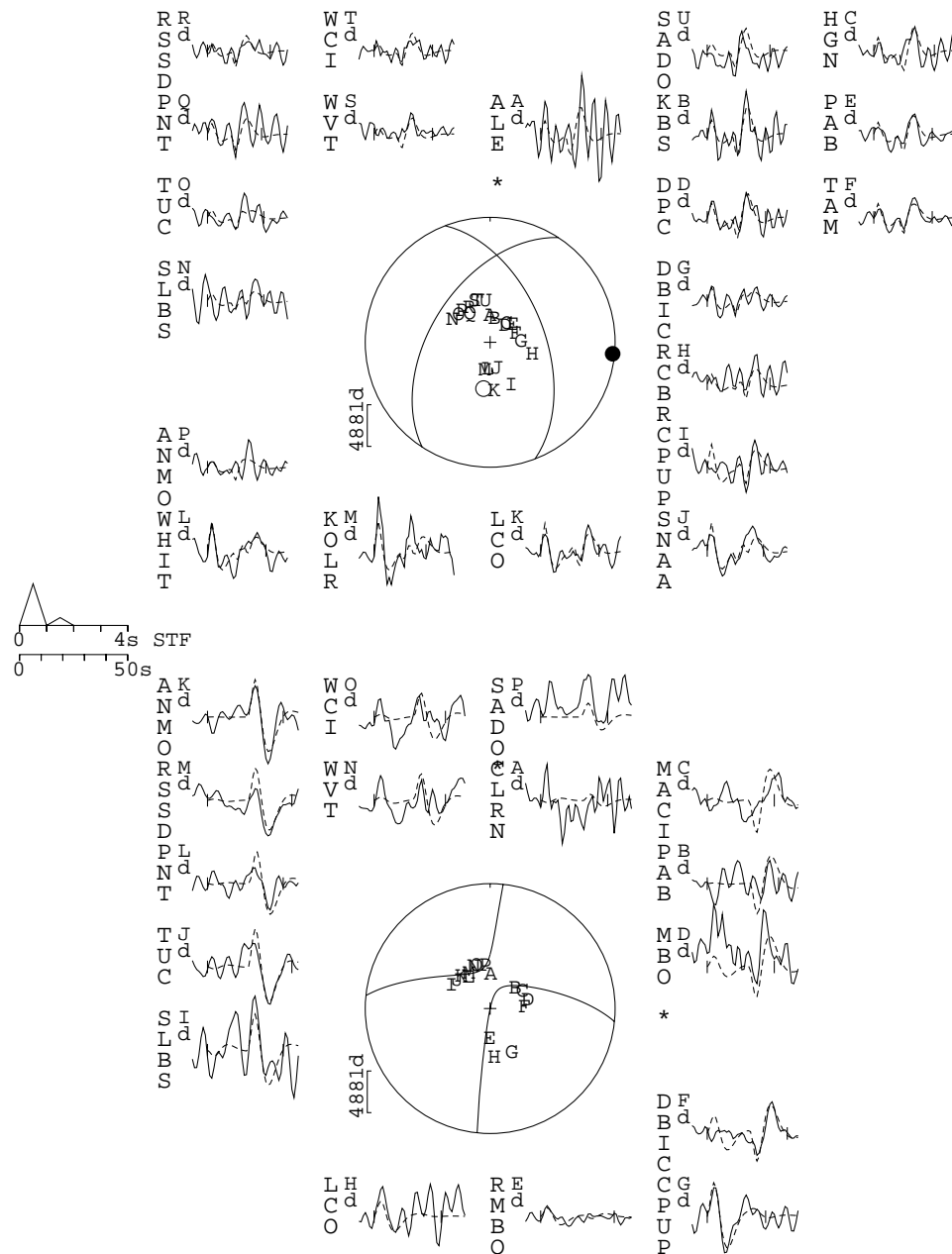


**Supplementary Figure 31:** Minimum misfit long-period teleseismic body-waveform model for the 13th November 2015 earthquake. The body-waves provide poor constraints on the strike, dip and rake, due to strong trade-offs and the limited azimuthal station distribution. The depth is well constrained, as the depth phases are separated from the direct arrivals.

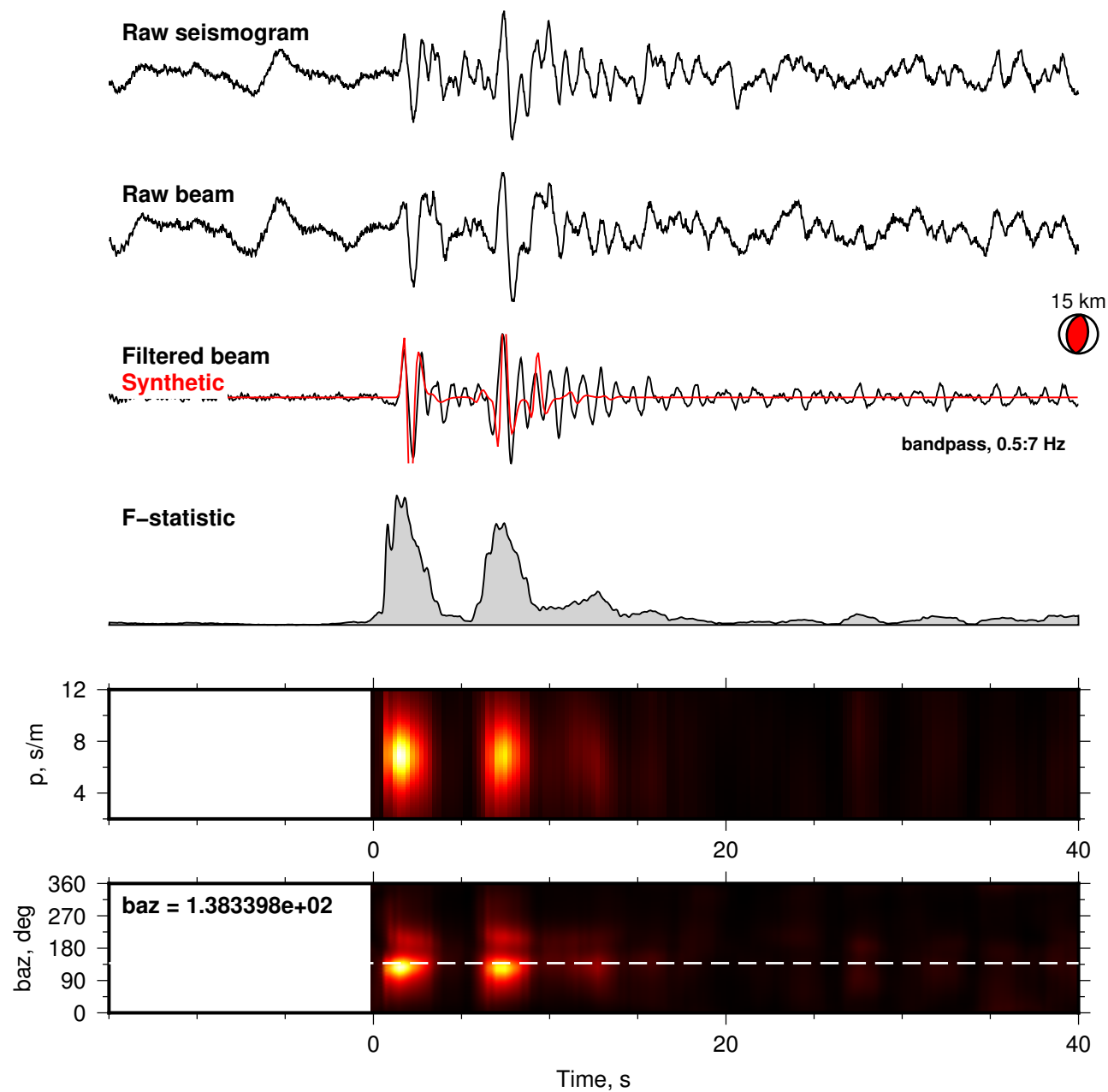


**Supplementary Figure 32:** Broadband vertical-component seismograms (black) and synthetics (red) for the 22nd May 2016 earthquake.

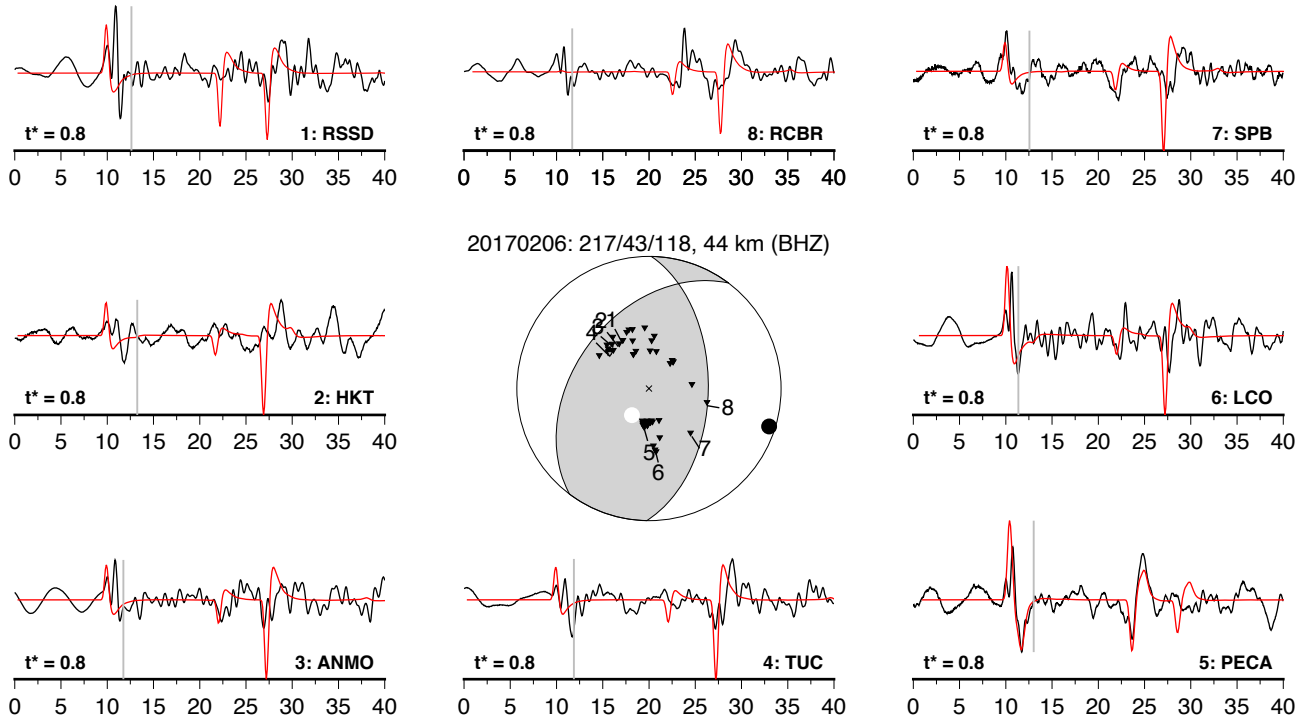
# 2016/10/31 - Mw 5.6 Colombia 213/51/131/40/2E17



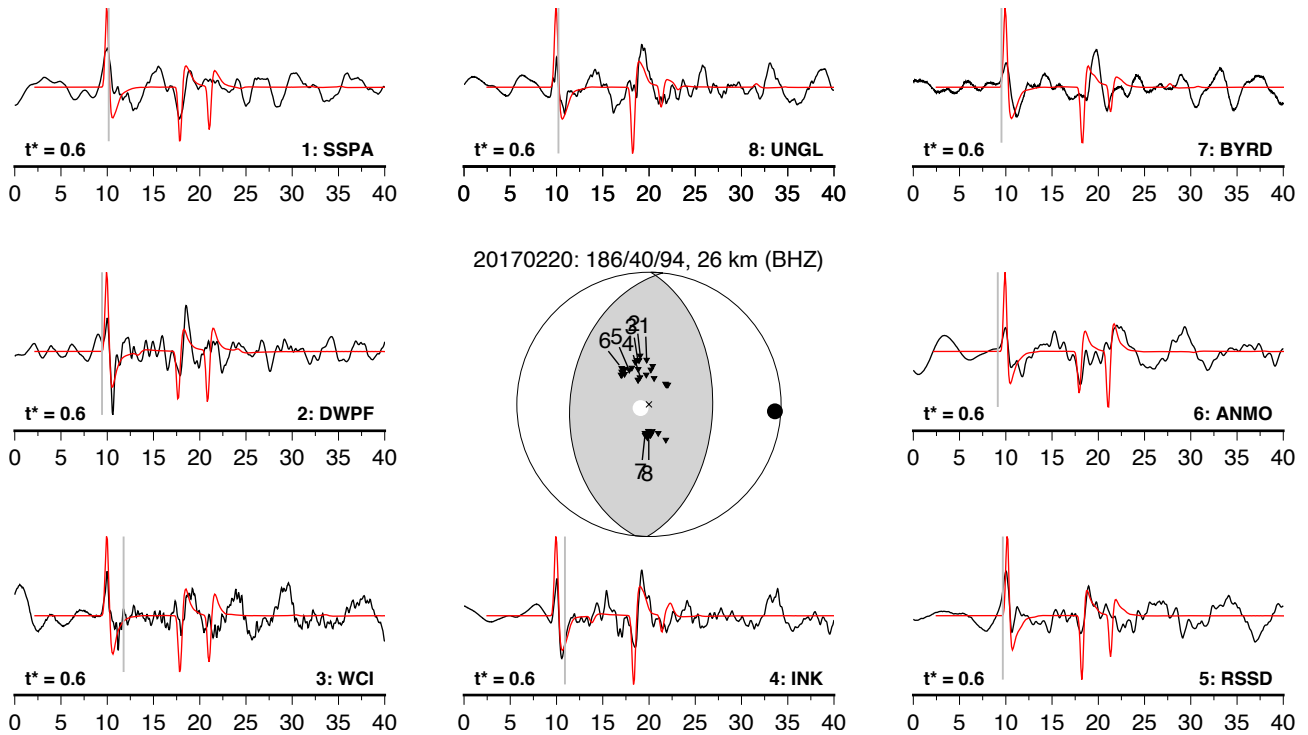
**Supplementary Figure 33:** Minimum misfit long-period teleseismic body-waveform model for the 31st October 2016 earthquake. The strike, dip and rake were fixed to the gCMT best double-couple and only the depth was solved for. A number of stations have small amplitude direct arrivals, but the depth phases are far larger amplitude, placing good constraints on the centroid depth.



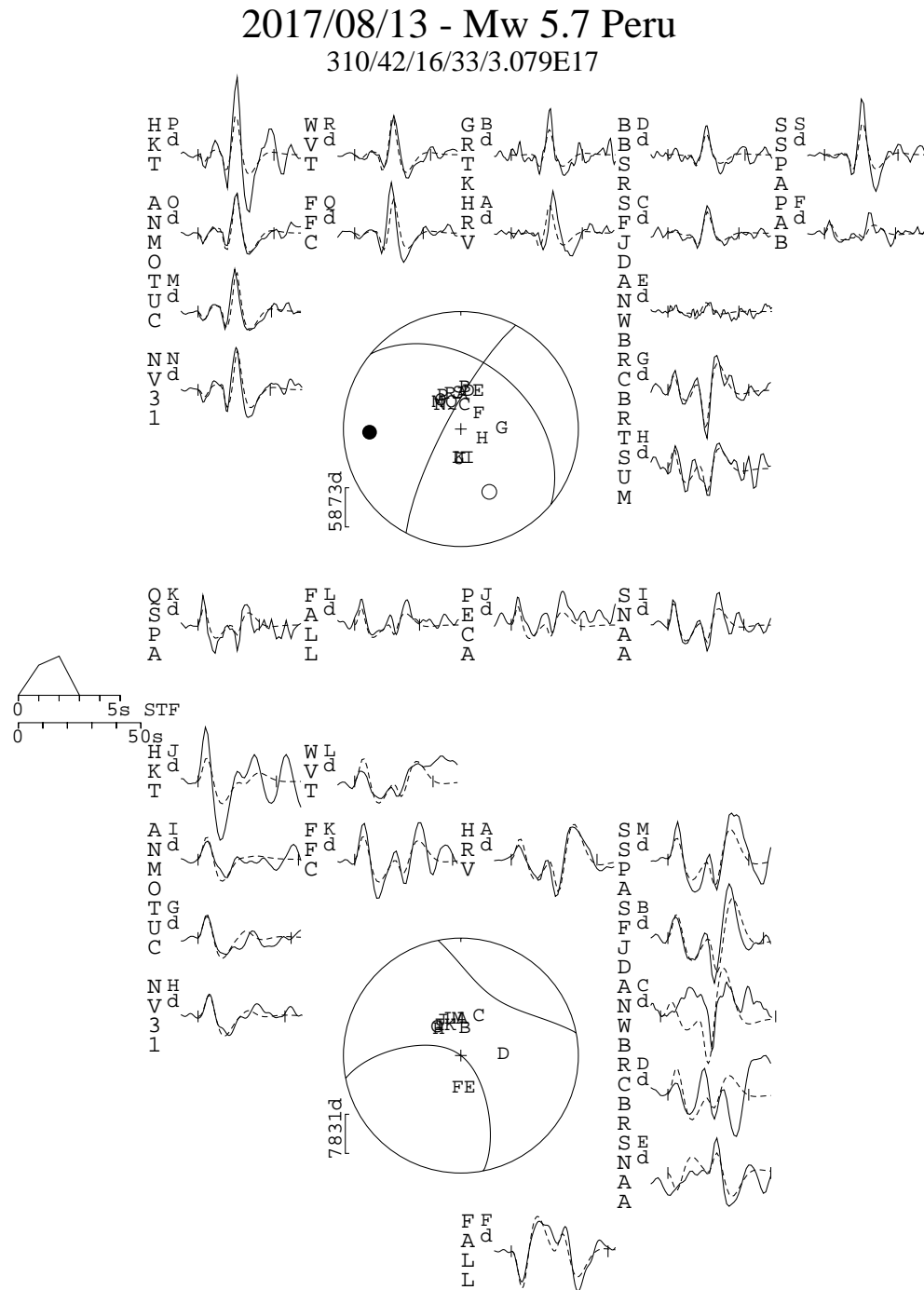
**Supplementary Figure 34:** Stacked short-period vertical-component seismograms (black) and synthetics (red) for the 12th December 2016 earthquake.



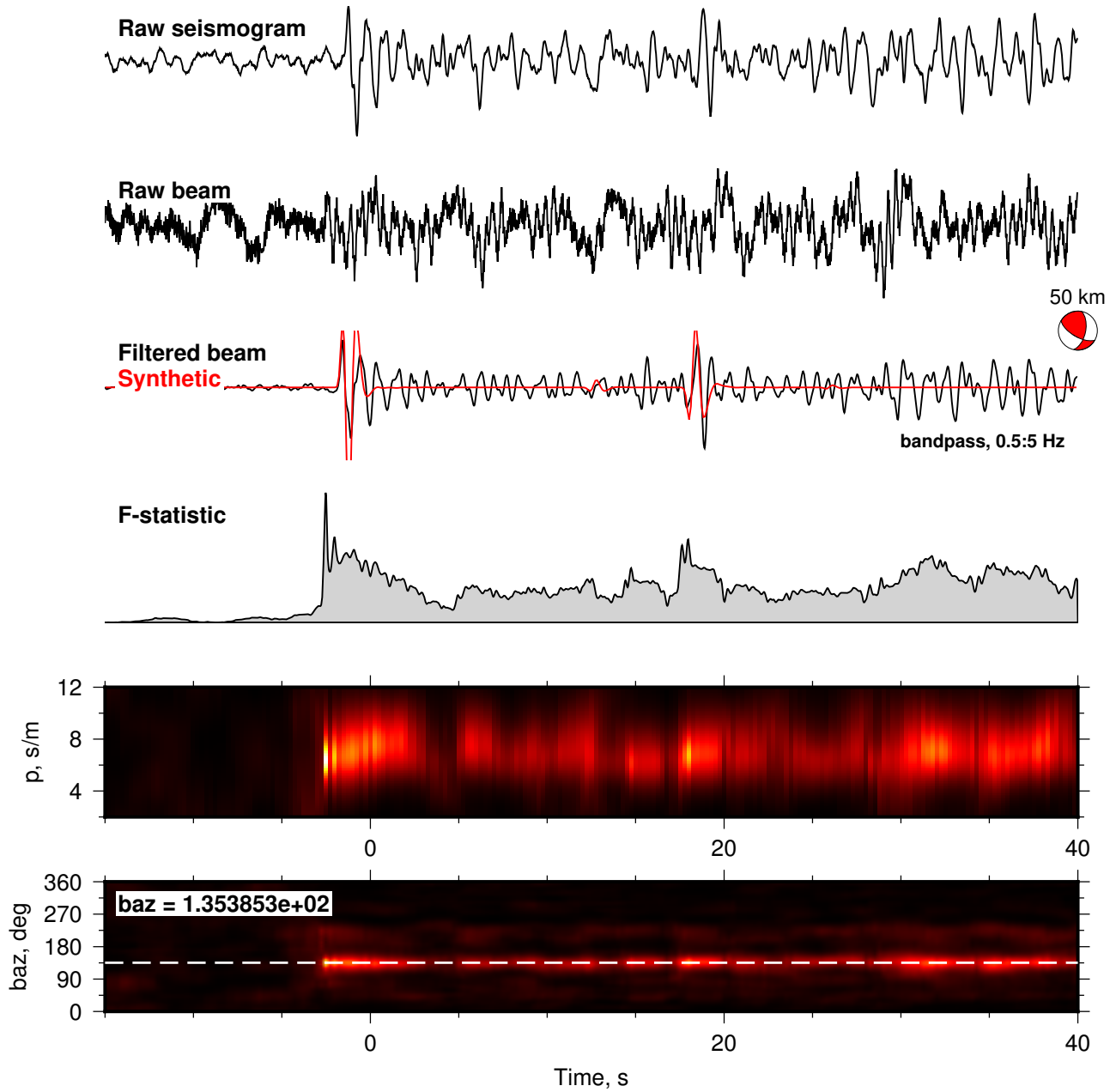
**Supplementary Figure 35:** Broadband vertical-component seismograms (black) and synthetics (red) for the 6th February 2017 earthquake. The double-pulse first arrival and broad wavelength of the depth phases suggests this event may have had a slightly more complex source-time function than assumed. I account for this in the estimate of the uncertainties.



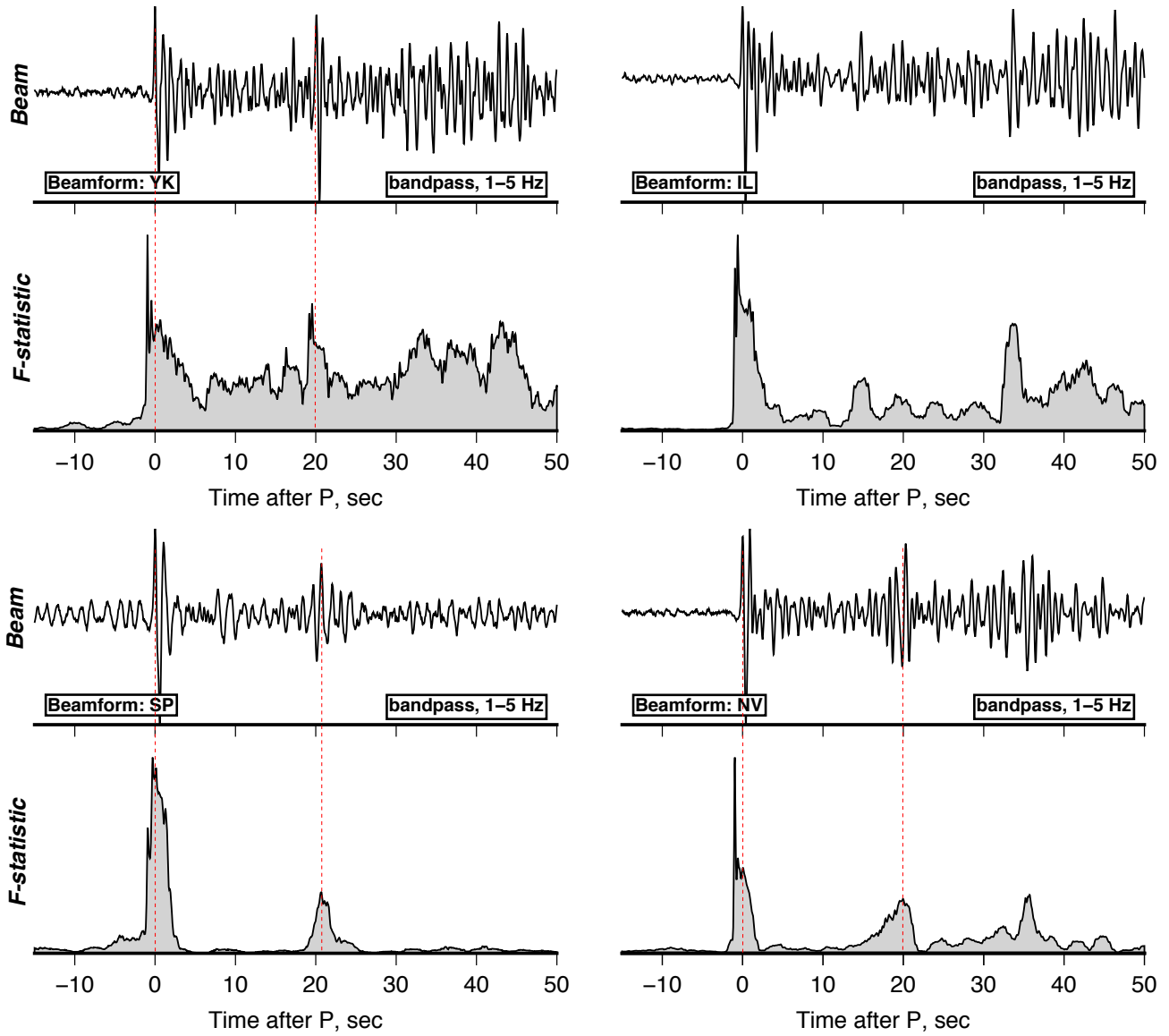
**Supplementary Figure 36:** Broadband vertical-component seismograms (black) and synthetics (red) for the 20th February 2017 earthquake.



**Supplementary Figure 37:** Minimum misfit long-period teleseismic body-waveform model for the 13th August 2017 earthquake. The *pP* phase is particularly clear at a number of stations in the NW of the focal sphere, placing excellent constraints on the earthquake centroid depth.



**Supplementary Figure 38:** Stacked short-period vertical-component seismograms (black) and synthetics (red) for the 19th July 2017 earthquake from the Yellowknife array. Additional beams from three other array sites are shown in Supplementary Figure 39 to demonstrate that the arrival at  $\sim 20$  s is consistent with being the  $sP$  depth phase.

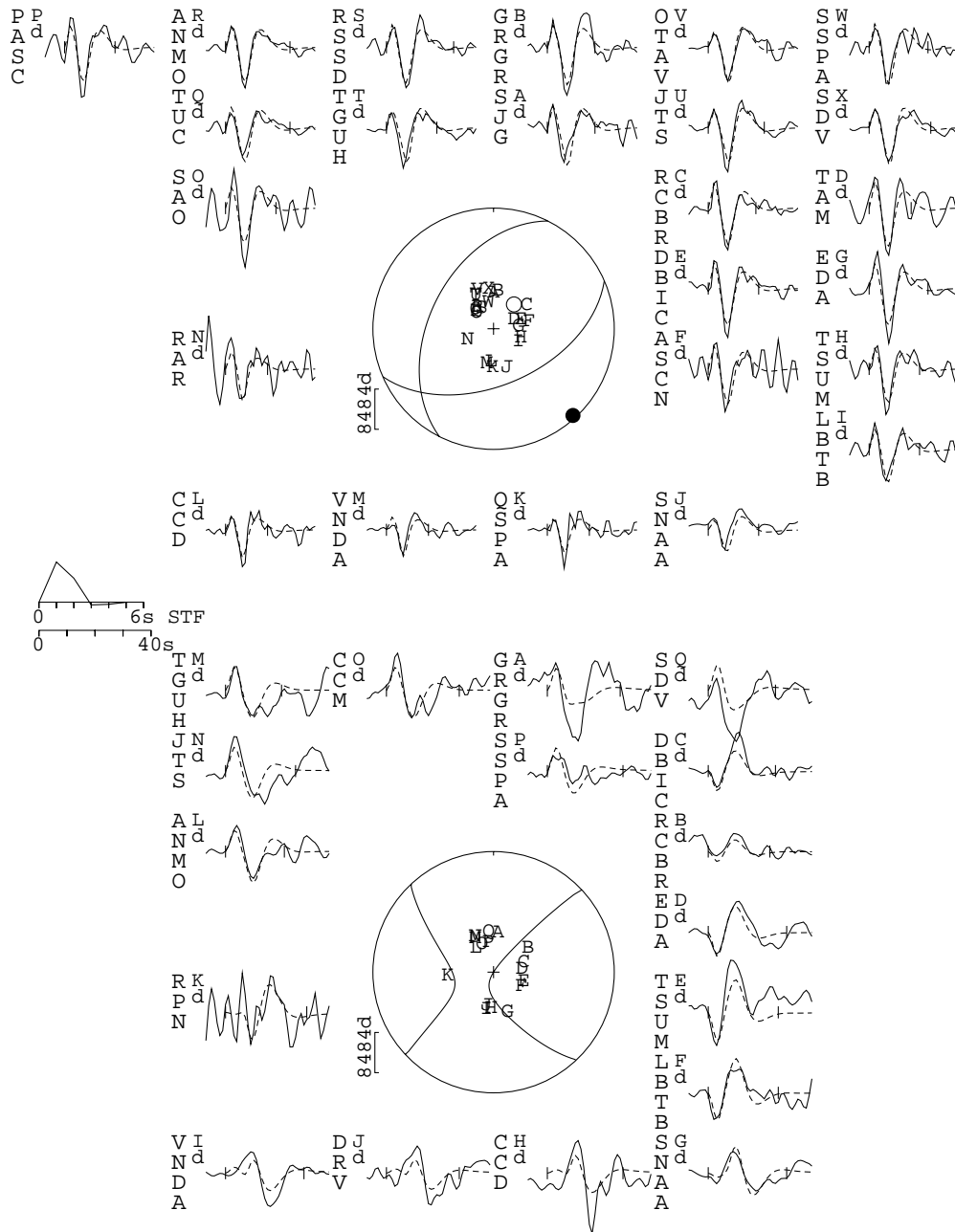


**Supplementary Figure 39:** Beam and F-statistic for four small-aperture arrays (YK: Yellowknife, SP: Spitsbergen, NV: Nevada, IL: ILAR). The red-dashed line shows the distinct peak in the F-statistic at  $\sim 20$ -21 s, which is consistent across three of the four arrays.



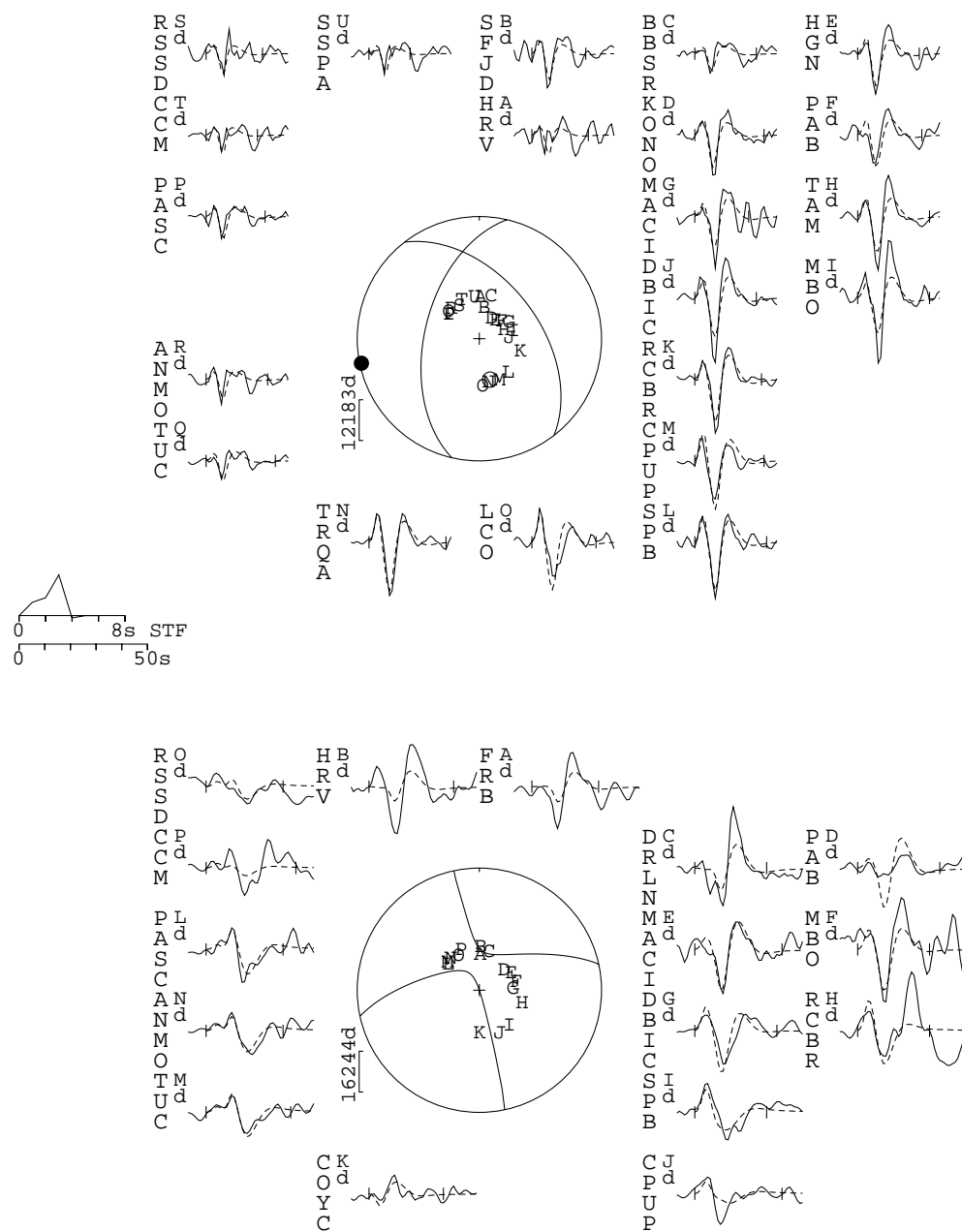
# 2019/11/19 - Mw 5.7 Argentina

207/46/60/14/3.219E17

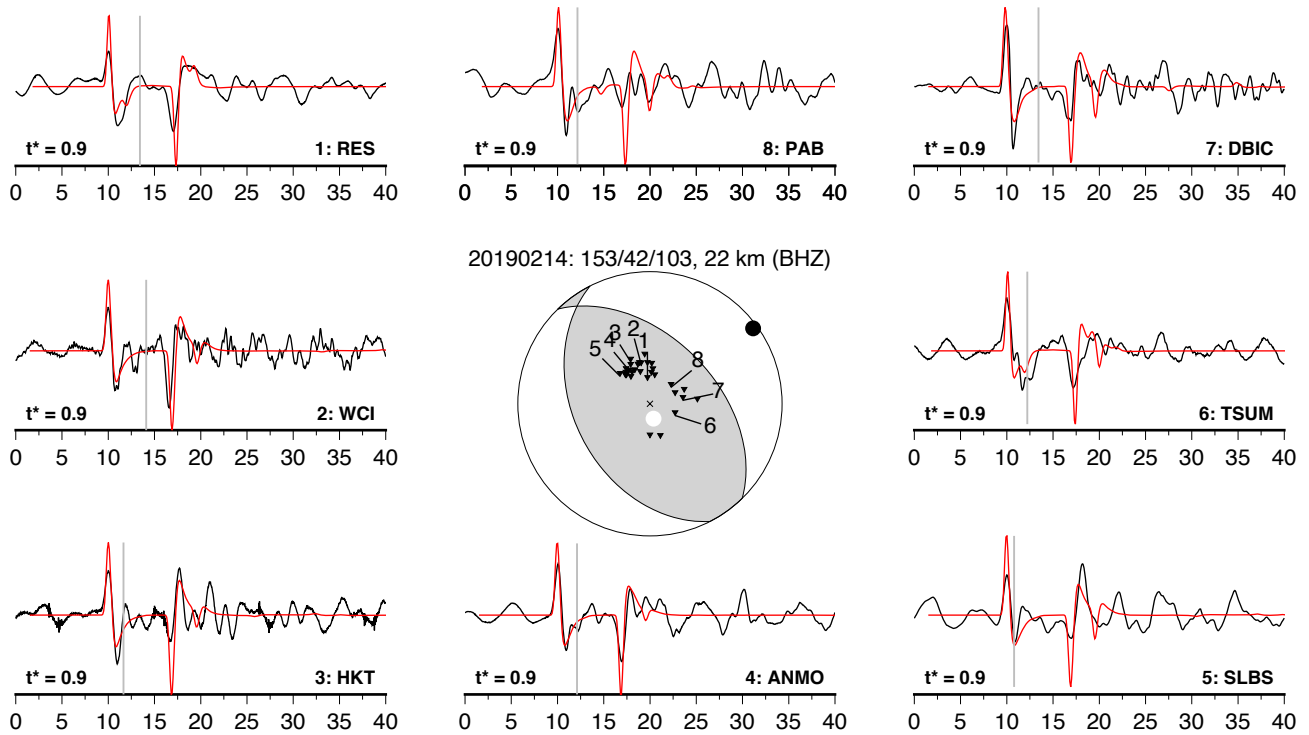


**Supplementary Figure 40:** Minimum misfit long-period teleseismic body-waveform model for the 19th November 2019 earthquake.

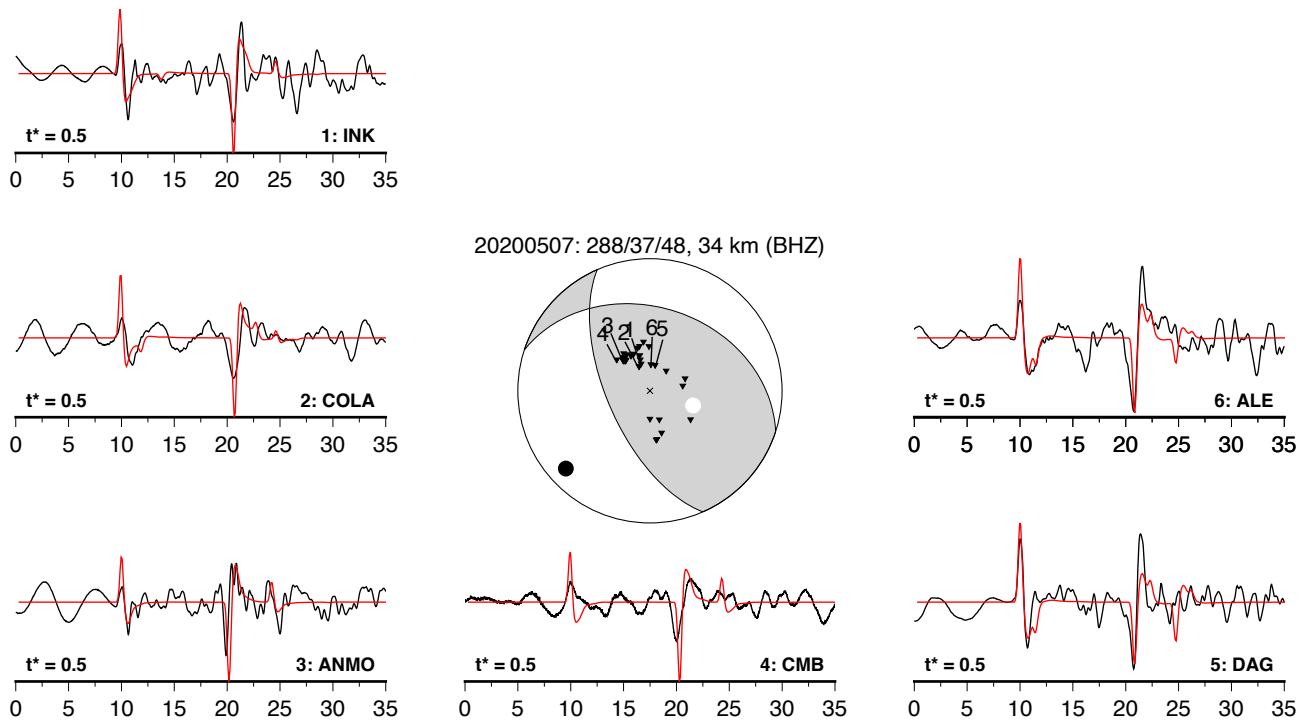
# 2019/12/24 - Mw 5.9 Colombia 193/53/126/12/6.647E17



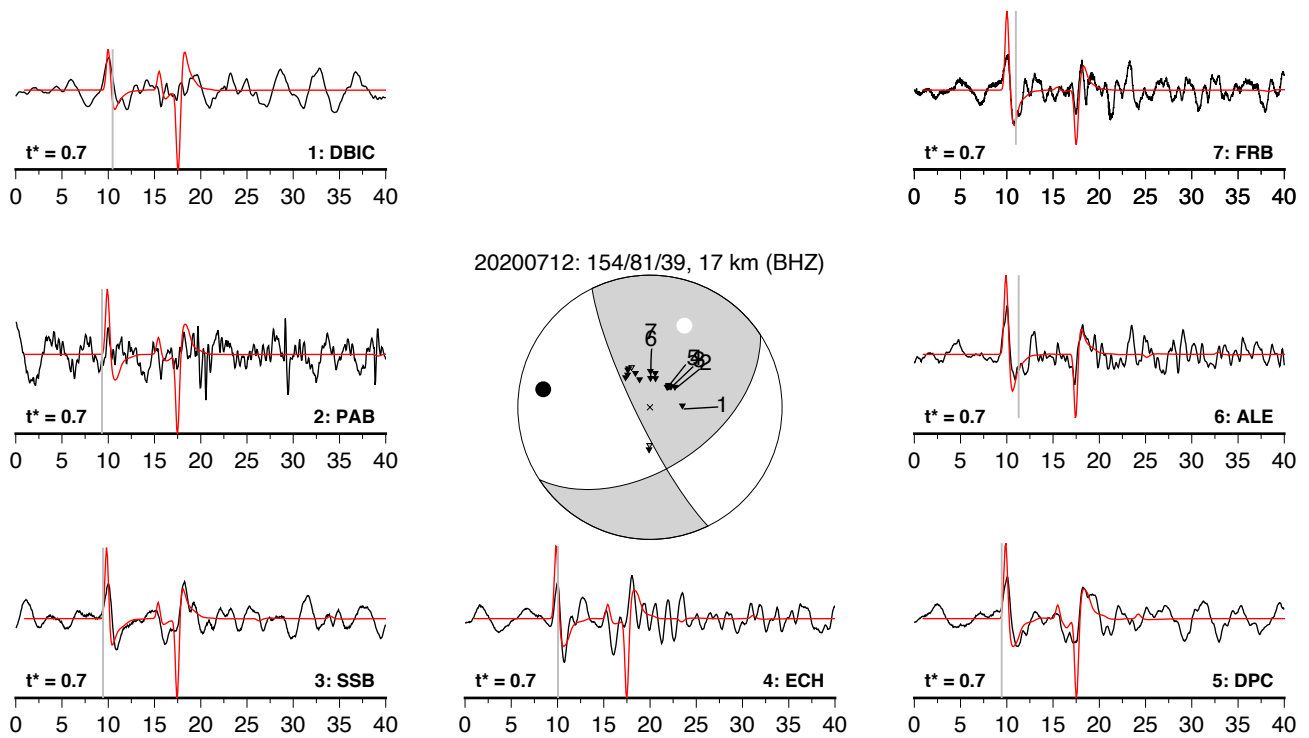
**Supplementary Figure 41:** Minimum misfit long-period teleseismic body-waveform model for the 24th December 2019 earthquake.



**Supplementary Figure 42:** Broadband vertical-component seismograms (black) and synthetics (red) for the 14th February 2019 earthquake.

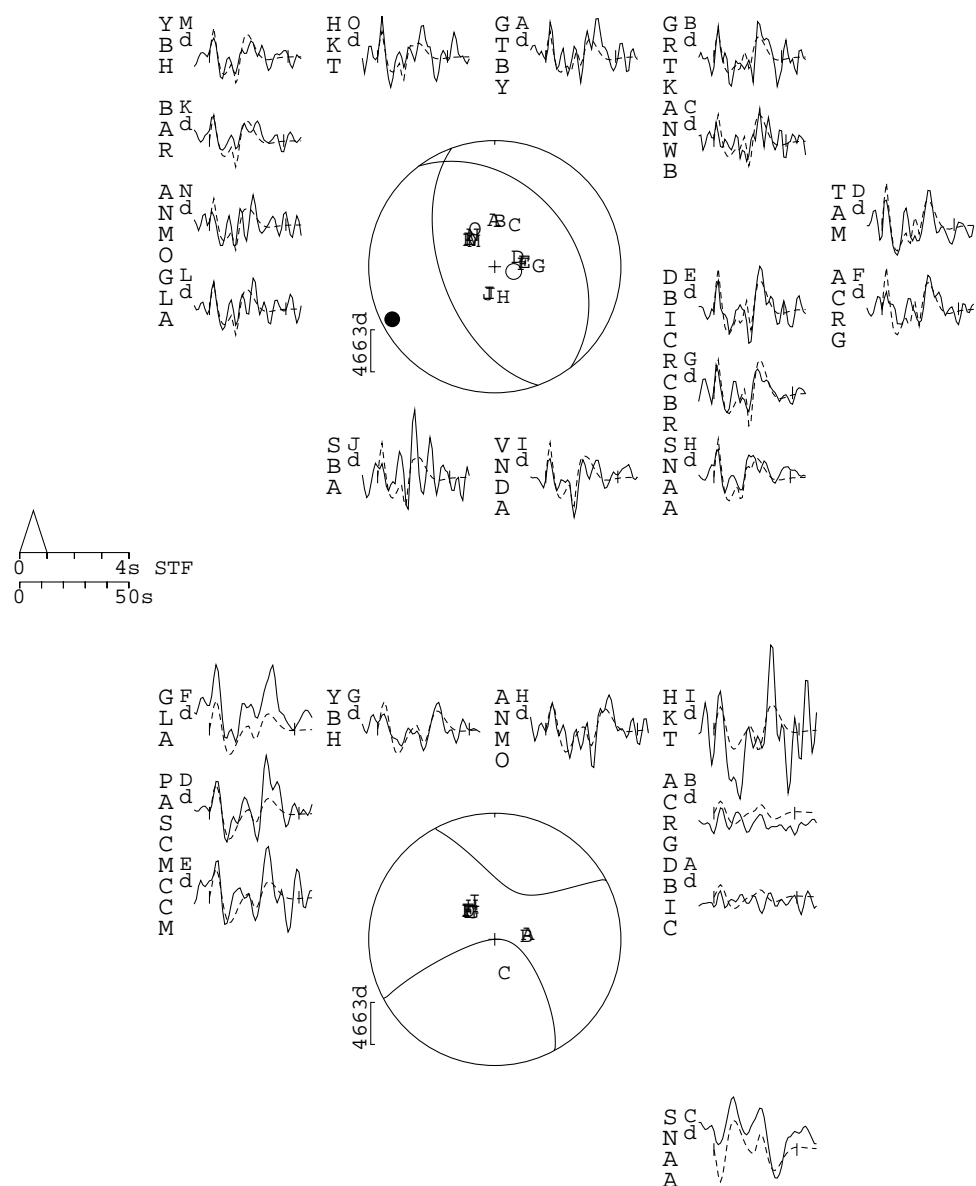


**Supplementary Figure 43:** Broadband vertical-component seismograms (black) and synthetics (red) for the 7th May 2020 earthquake.



**Supplementary Figure 44:** Broadband vertical-component seismograms (black) and synthetics (red) for the 12th July 2020 earthquake.

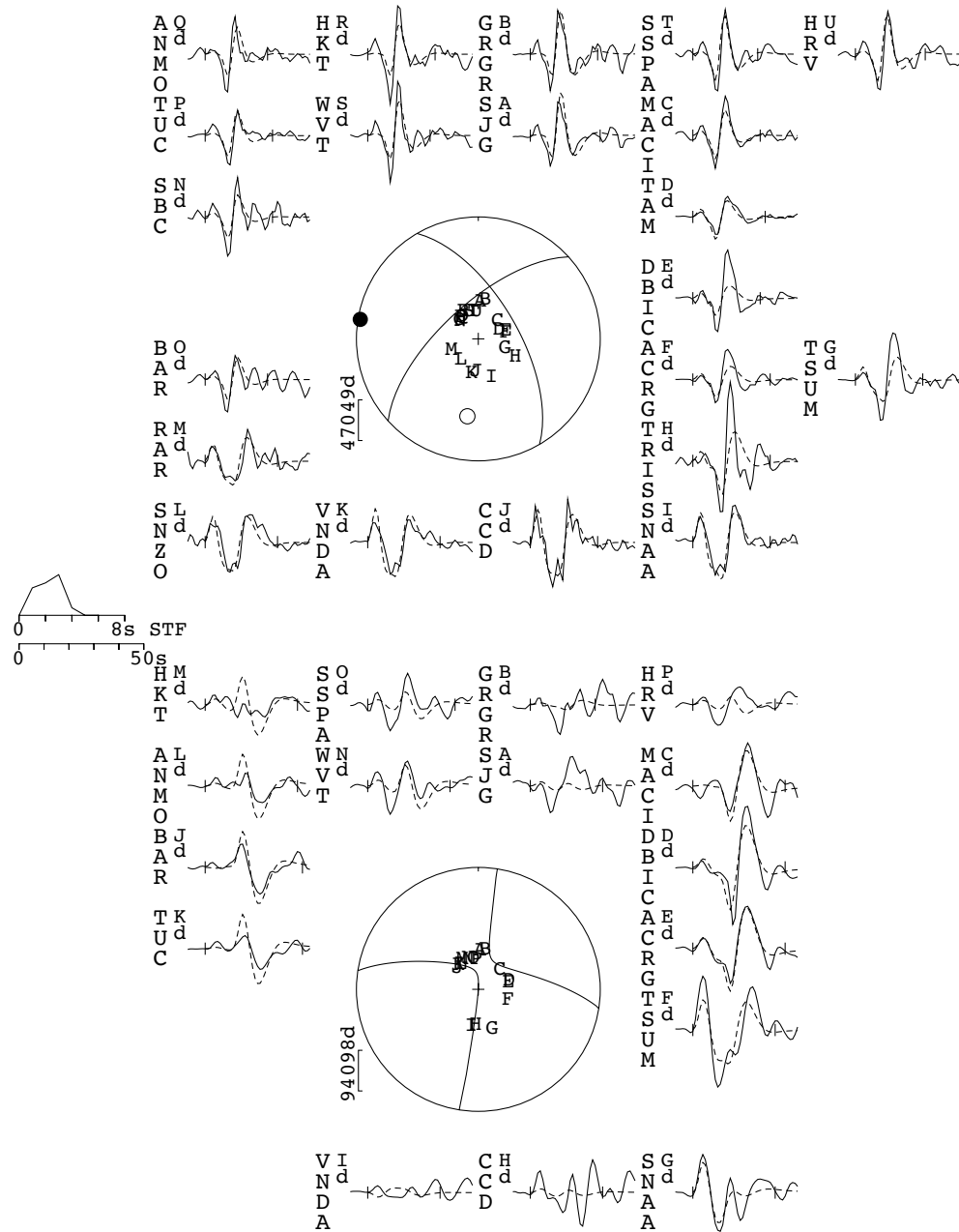
2020/10/20 - Mw 5.5 Central Peru  
160/55/100/37/2.5E17



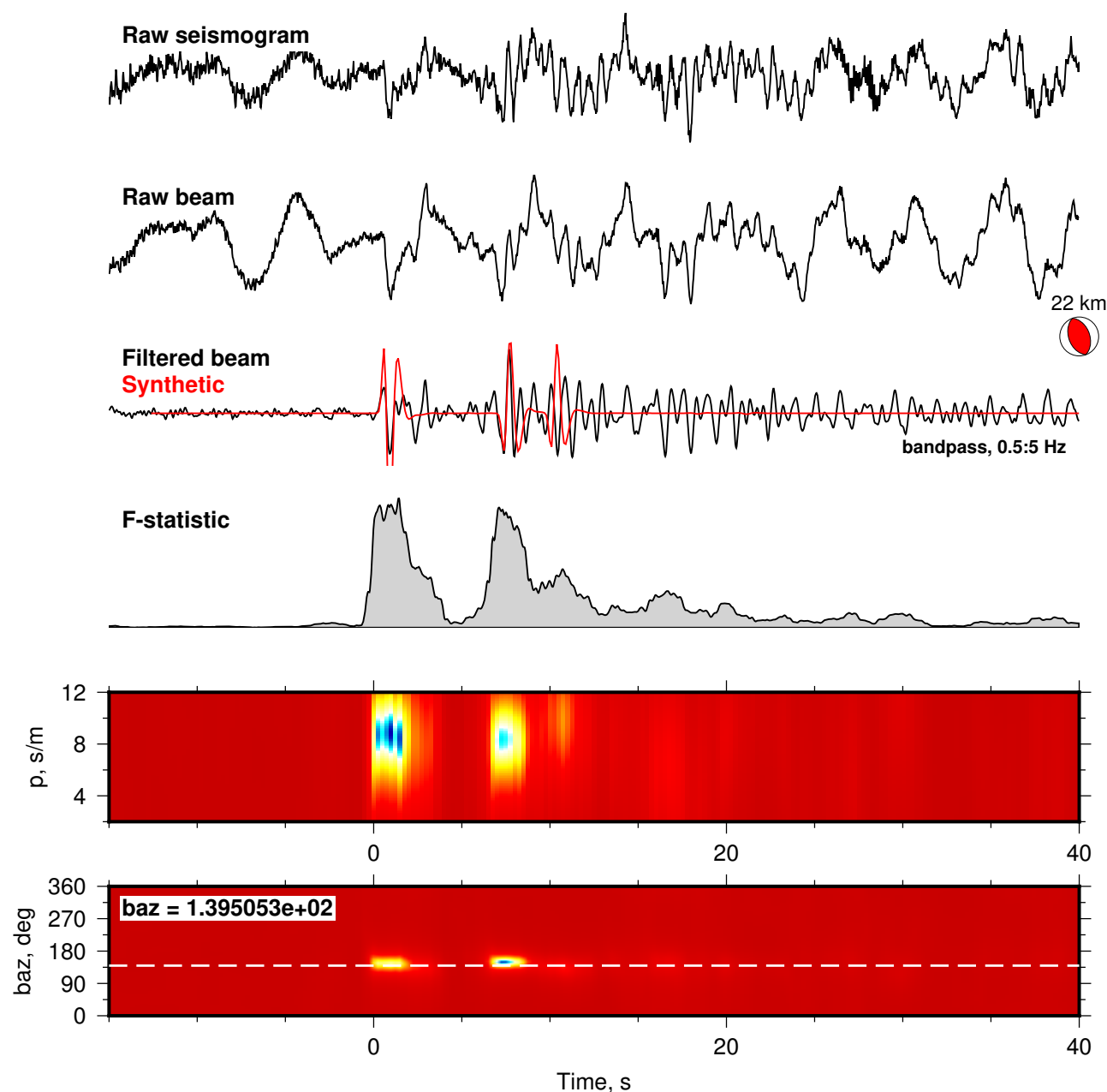
**Supplementary Figure 45:** Minimum misfit long-period teleseismic body-waveform model for the 30th October 2020 earthquake.

# 2021/01/19 - Mw 6.4 Argentina

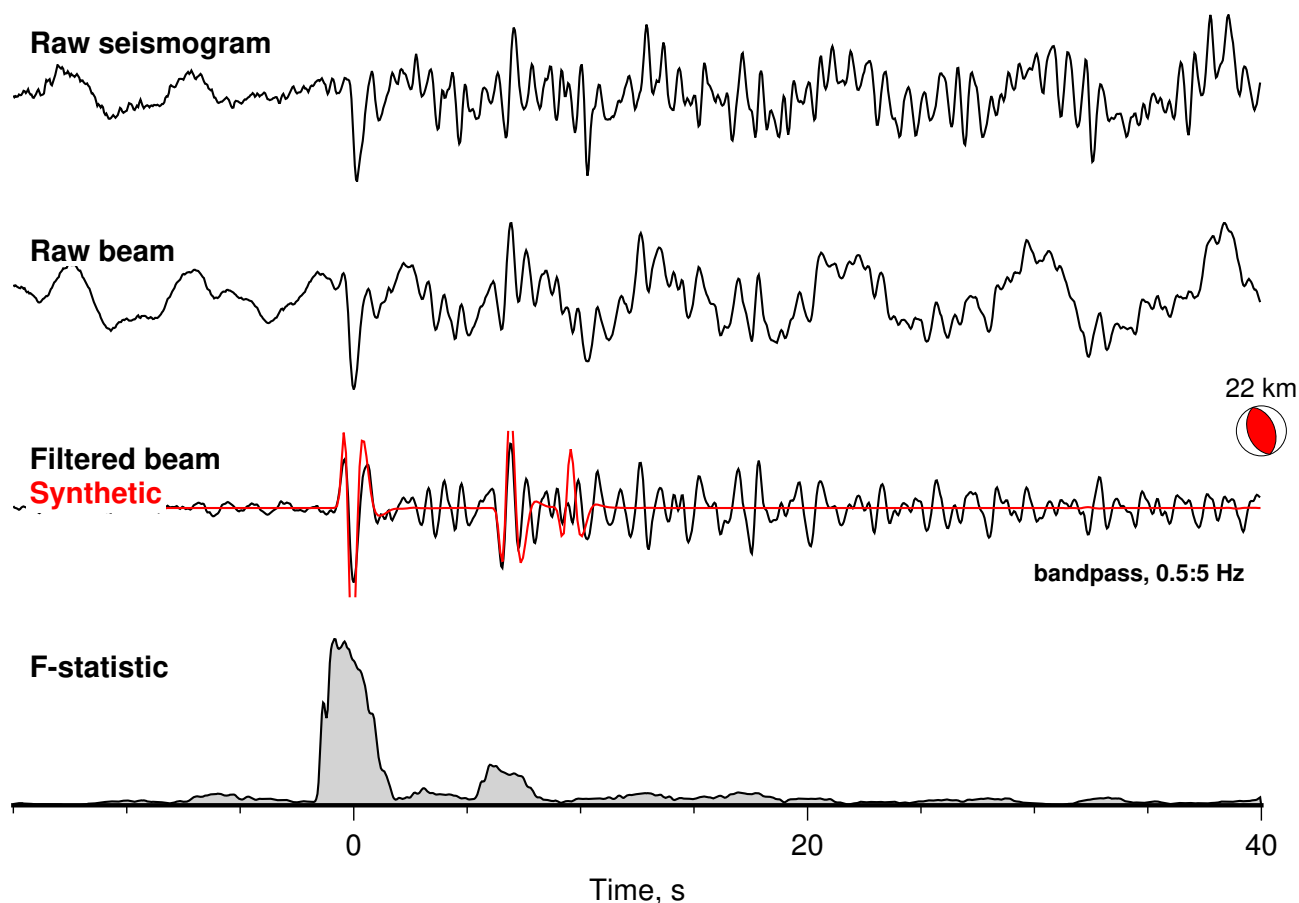
228/67/151/22/4.415E18



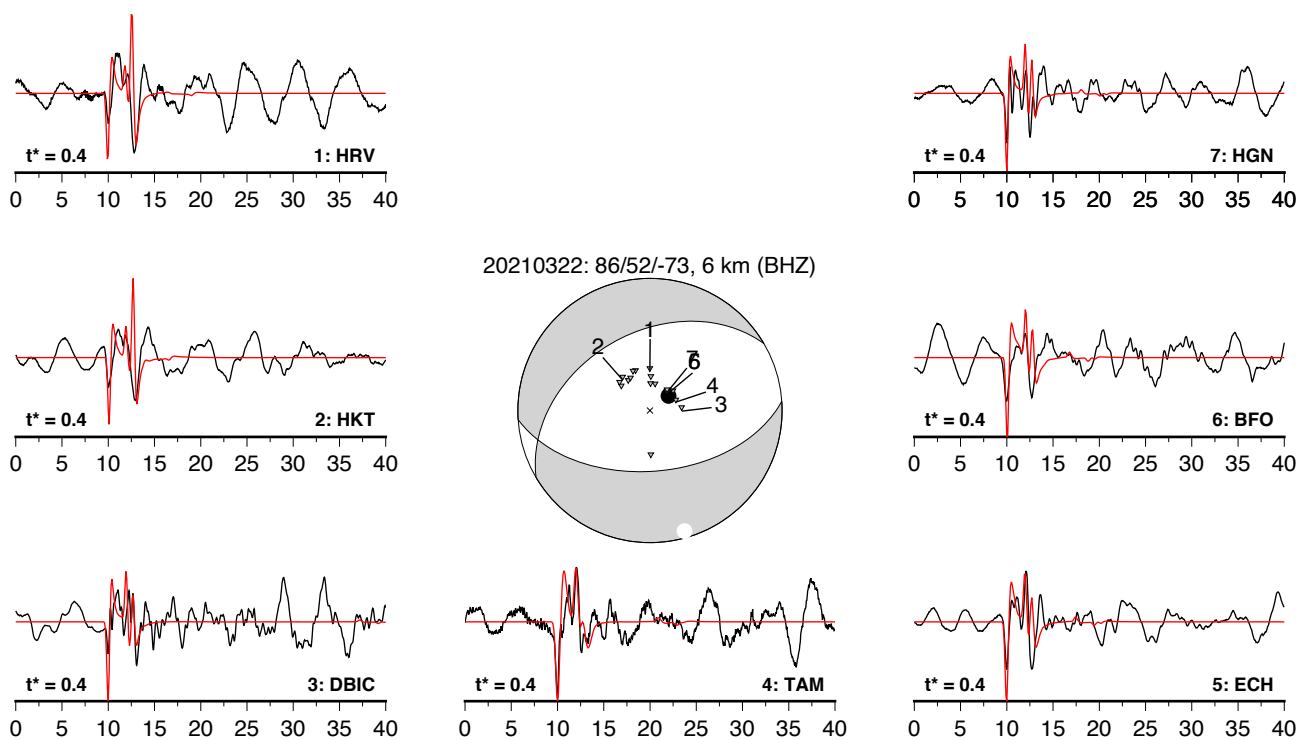
**Supplementary Figure 46:** Minimum misfit long-period teleseismic body-waveform model for the 19th January 2021 earthquake.



**Supplementary Figure 47:** Stacked short-period vertical-component seismograms (black) and synthetics (red) for the 9th February 2021 earthquake from the Lajitas array in North America. Coherent energy arrives  $\sim 7$  s after the direct  $P$ -arrival, and the beamforming indicates this energy derives from the same back-azimuth as the earthquake. Beamformed seismograms from the Pinedale array also show a distinct arrival at the same time  $\sim 8$  s after the direct  $P$  (see Supplementary Figure 48). The mechanism was assumed based on the mechanisms of nearby seismicity. I interpret the arrival to be the  $pP$  depth phase, as there is no clear energy arriving before it in the  $P$ -wave coda.



**Supplementary Figure 48:** Stacked short-period vertical-component seismograms (black) and synthetics (red) for the 9th February 2021 earthquake from the Pinedale array in North America.

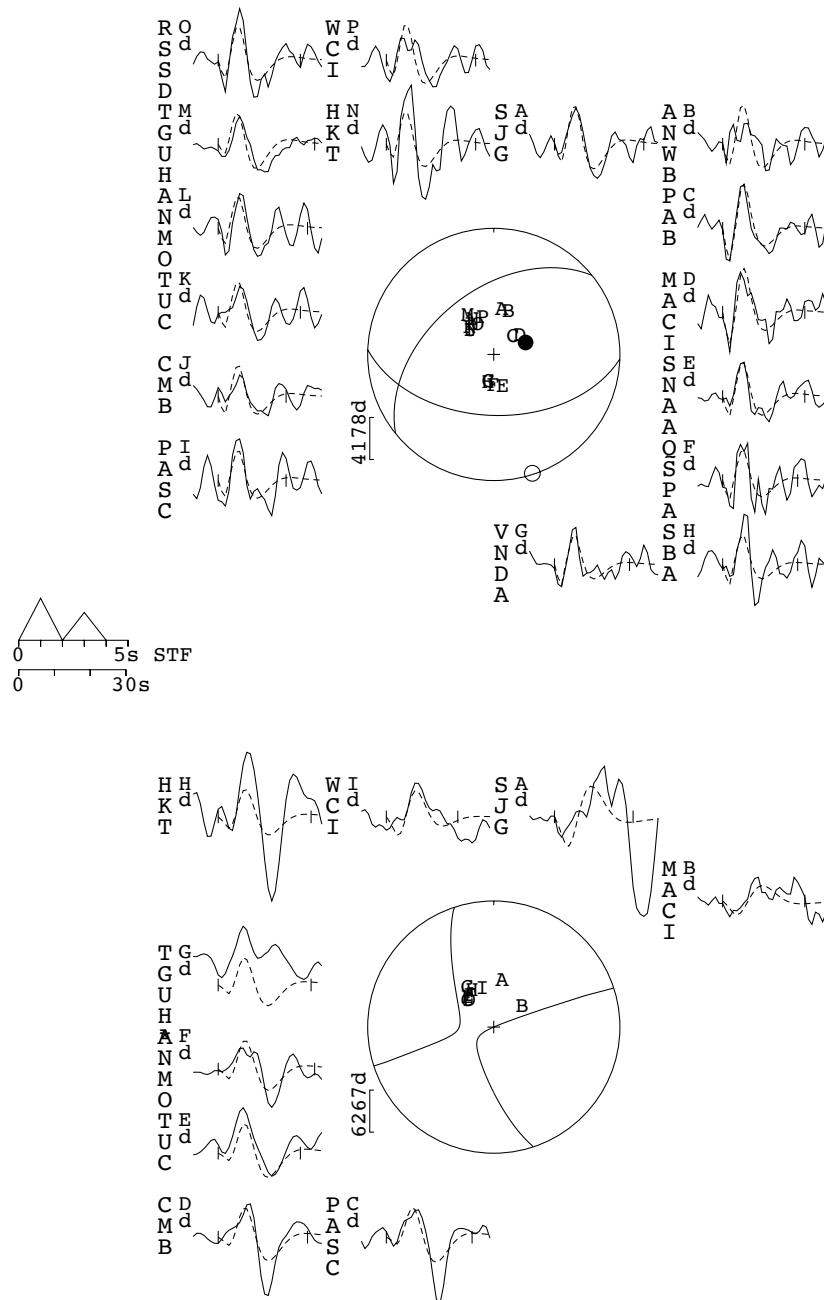


**Supplementary Figure 49:** Broadband vertical-component seismograms (black) and synthetics (red) for the 22nd March 2021 earthquake.



## 10/10/2021 - Mw 5.6 South Peru

92/50/299/7/2.893E17



**Supplementary Figure 50:** Minimum misfit long-period teleseismic body-waveform model for the 10th October 2021 earthquake in south Peru. The strike and rake of this mechanism are particularly poorly constrained, therefore no estimate on their uncertainties has been provided. The *SH* waves for station TGUH were not included in the inversion misfit estimate.

## References

- Abers, G. and McCaffrey, R. (1988). Active deformation in the New Guinea fold-and-thrust-belt: seismological evidence for strike-slip faulting and basement-involved thrusting. *J. Geophys. Res.*, 93(B11):13332–13354.
- Alvarado, P., Beck, S., Zandt, G., Araujo, M., Triep, E., Isacks, B. L., Araujo, M., Puebla, N. P., and Sistena, J. A. (2005). Crustal deformation in the south-central Andes backarc terranes as viewed from regional broad-band seismic waveform modelling. *Geophysical Journal International*, 163(2):580–598.
- Bouhifd, M., Andraut, D., Fiquet, G., and Richet, P. (1996). Thermal expansion of forsterite up to the melting point. *Geophysical Research Letters*, 23(10):1143–1146.
- Bown, J. W. and White, R. S. (1995). Effect of finite extension rate on melt generation at rifted continental margins. *Journal of Geophysical Research*, 100(B9):18011–18029.
- Cahill, T., Isacks, B. L., Whitman, D., Chatelain, J. ., Perez, A., and Chiu, J. M. (1992). Seismicity and tectonics in Jujuy Province, northwestern Argentina. *Tectonics*, 11(5):944–959.
- Chapman, C. H. (1978). A new method for computing synthetic seismograms. *Geophysical Journal International*, 54(3):481–518.
- Christensen, D. H. and Ruff, L. J. (1985). Analysis of the trade-off between hypocentral depth and source time function. *Bulletin of the Seismological Society of America*, 75(6):1637–1656.
- Condori, C., França, G. S., Tavera, H. J., Albuquerque, D. F., Bishop, B. T., and Beck, S. L. (2017). Crustal structure of north Peru from analysis of teleseismic receiver functions. *Journal of South American Earth Sciences*, 76:11–24.
- Craig, T. J., Copley, A., and Jackson, J. A. (2012). Thermal and tectonic consequences of India underthrusting Tibet. *Earth and Planetary Science Letters*, 353-354:231–239.
- Devlin, S., Isacks, B. L., Pritchard, M. E., Barnhart, W. D., and Lohman, R. B. (2012). Depths and focal mechanisms of crustal earthquakes in the central Andes determined from teleseismic waveform analysis and InSAR. *Tectonics*, 31(2):1–33.
- Dimate, C., Rivera, L., Taboada, A., Delouis, B., Osorio, A., Jimenez, E., Fuenzalida, A., Cisternas, A., and Gomez, I. (2003). The 19 January 1995 Tauramena (Colombia) earthquake: Geometry and stress regime. *Tectonophysics*, 363(3-4):159–180.
- Dorbath, C., Dorbath, L., Cisternas, A., Deverchere, J., Diament, M., Ocola, L., and Morales, M. (1986). On crustal seismicity of the Amazonian foothill of the central Peruvian Andes. *Geophysical Research Letters*, 13(10):1023–1026.
- Dorbath, L., Dorbath, C., Jimenez, E., and Rivera, L. (1991). Seismicity and tectonic deformation in the Eastern Cordillera and the sub-Andean zone of central Peru. *Journal of South American Earth Sciences*, 4(1-2):13–24.
- Dziewonski, A. M., Chou, T.-A., and Woodhouse, J. H. (1981). Determination of earthquake source parameters from waveform data for studies of global and regional seismicity. *Journal of Geophysical Research: Solid Earth*, 86(B4):2825–2852.

- Ekström, G., Nettles, M., and Dziewoński, A. (2012). The global CMT project 20042010: Centroid-moment tensors for 13,017 earthquakes. *Physics of the Earth and Planetary Interiors*, 200:1–9.
- Forsyth, D. W. (1982). Determinations of focal depths of earthquakes associated with the bending of oceanic plates at trenches. *Physics of the Earth and Planetary Interiors*, 28(2):141–160.
- Futterman, W. I. (1962). Dispersive body waves. *Journal of Geophysical Research*, 67(13):5279–5291.
- Grose, C. J. and Afonso, J. C. (2013). Comprehensive plate models for the thermal evolution of oceanic lithosphere. *Geochemistry, Geophysics, Geosystems*, 14(9):3751–3778.
- Hayes, G. P., Moore, G. L., Portner, D. E., Hearne, M., Flamme, H., Furtney, M., and Smoczyk, G. M. (2018). Slab2, a comprehensive subduction zone geometry model. *Science*, 362(6410):58–61.
- Heyburn, R. and Bowers, D. (2008). Earthquake depth estimation using the F trace and associated probability. *Bulletin of the Seismological Society of America*, 98(1):18–35.
- Jackson, J. A., Priestley, K., Allen, M., and Berberian, M. (2002). Active tectonics of the South Caspian Basin. *Geophysical Journal International*, 148(2):214–245.
- James, D. E. and Snoke, J. A. (1994). Structure and tectonics in the region of flat subduction beneath central Peru: Crust and uppermost mantle. *Journal of Geophysical Research*, 99(B4):6899.
- Kennett, B. L. N., Engdahl, E. R., and Buland, R. (1995). Constraints on seismic velocities in the Earth from traveltimes. *Geophysical Journal International*, 122(1):108–124.
- Legrand, D., Baby, P., Bondoux, F., Dorbath, C., Bès de Berc, S., and Rivadeneira, M. (2005). The 1999-2000 seismic experiment of Macas swarm (Ecuador) in relation with rift inversion in Subandean foothills. *Tectonophysics*, 395(1-2):67–80.
- Maggi, A., Jackson, J. A., Priestley, K., and Baker, C. (2000). A re-assessment of focal depth distributions in southern Iran, the Tien Shan and northern India: do earthquakes really occur in the continental mantle? *Geophysical Journal International*, 143(3):629–661.
- Mareschal, J. C. and Jaupart, C. (2013). Radiogenic heat production, thermal regime and evolution of continental crust.
- McCaffrey, R. and Abers, G. (1988). Syn3: a program for inversion of teleseismic body waveforms on microcomputers.
- McGroder, M. F., Lease, R. O., and Pearson, D. M. (2015). Along-strike variation in structural styles and hydrocarbon occurrences, Subandean fold-and-thrust belt and inner foreland, Colombia to Argentina. In DeCelles, P. G., Ducea, M. N., Carrapa, B., and Kapp, P. A., editors, *Geodynamics of a Cordilleran Orogenic System: The Central Andes of Argentina and Northern Chile*. Geological Society of America.
- McKenzie, D. (1978). Some remarks on the development of sedimentary basins. *Earth and Planetary Science Letters*, 40(1):25–32.
- McKenzie, D., Jackson, J., and Priestley, K. (2005). Thermal structure of oceanic and continental lithosphere. *Earth and Planetary Science Letters*, 233(3):337–349.

- 248 Nabalek, J. (1984). *Determination of earthquake source parameters from inversion of body waves*. PhD  
249 thesis, Massachusetts Institute of Technology.
- 250 Ojeda, A. and Havskov, J. (2001). Crustal structure and local seismicity in Colombia. *Journal of*  
251 *Seismology*, 5(4):575–593.
- 252 Poveda, E., Monsalve, G., and Vargas, C. A. (2015). Receiver functions and crustal structure of the  
253 northwestern Andean region, Colombia. *Journal of Geophysical Research: Solid Earth*, 120(4):2408–  
254 2425.
- 255 Priestley, K. and McKenzie, D. (2013). The relationship between shear wave velocity, temperature,  
256 attenuation and viscosity in the shallow part of the mantle. *Earth and Planetary Science Letters*,  
257 381:78–91.
- 258 Ryan, J., Beck, S., Zandt, G., Wagner, L., Minaya, E., and Tavera, H. (2016). Central Andean crustal  
259 structure from receiver function analysis. *Tectonophysics*, 682:120–133.
- 260 Salfity, J. A. and Marquillas, R. A. (1994). Tectonic and Sedimentary Evolution of the Cretaceous-  
261 Eocene Salta Group Basin, Argentina. In Salfity, J. A., editor, *Cretaceous Tectonics of the Andes*,  
262 pages 266–315. Vieweg.
- 263 Sandiford, M. (1999). Mechanics of basin inversion. *Tectonophysics*, 305(1-3):109–120.
- 264 Smalley, R. and Isacks, B. L. (1990). Seismotectonics of thin- and thick-skinned deformation in  
265 the Andean foreland from local network data: evidence for a seismogenic lower crust. *Journal of*  
266 *Geophysical Research*, 95(B8):12487–12498.
- 267 Smalley, R., Pujol, J., Regnier, M., Chiu, J. ., Chatelain, J. ., Isacks, B. L., Araujo, M., and Puebla,  
268 N. (1993). Basement seismicity beneath the Andean precordillera thinskin thrust belt and  
269 implications for crustal and lithospheric behavior. *Tectonics*, 12(1):63–76.
- 270 Starck, D. (2010). Cuenca Cretácica-Paleógena Del Noroeste Argentino. In *VIII Congreso de Ex-*  
271 *ploración y Desarrollo de Hidrocarburos Simposio Cuencas Argentinas*, pages 407–453, Instituto  
272 Argentino del Petróleo y el Gas.
- 273 Suárez, G., Gagnepain, J., Cisternas, A., Hatzfeld, D., Molnar, P., Ocola, L., Roecker, S. W., and  
274 Viodé, J. P. (1990). Tectonic deformation of the Andes and the configuration of the subducted  
275 slab in central Peru; results from a microseismic experiment. *Geophysical Journal International*,  
276 103(1):1–12.
- 277 Taymaz, T., Jackson, J. A., and Westaway, R. (1990). Earthquake mechanisms in the Hellenic Trench  
278 near Crete. *Geophysical Journal International*, 102(3):695–731.
- 279 Vaca, S., Vallée, M., Nocquet, J. M., and Alvarado, A. (2019). Active deformation in Ecuador  
280 enlightened by a new waveform-based catalog of earthquake focal mechanisms. *Journal of South*  
281 *American Earth Sciences*, 93:449–461.
- 282 Weston, J., Engdahl, E. R., Harris, J., Di Giacomo, D., and Storchak, D. A. (2018). ISC-EHB:  
283 Reconstruction of a robust earthquake data set. *Geophysical Journal International*, 214(1):474–484.
- 284 Zwick, P., McCaffrey, R., and Abers, G. (1994). MT5 Program.